Development/Plasticity/Repair

Inositol Polyphosphate-5-Phosphatase K (*Inpp5k*) Enhances Sprouting of Corticospinal Tract Axons after CNS Trauma

Sierra D. Kauer,[1] Kathryn L. Fink,[1] Elizabeth H. F. Li,[1] Brian P. Evans,[2] Noa Golan,[1] and William B. J. Cafferty[1]

[1]Departments of Neurology and Neuroscience, Yale University School of Medicine, New Haven, Connecticut 06520, and [2]Regeneron Pharmaceuticals, Tarrytown, New York 10591

Failure of CNS neurons to mount a significant growth response after trauma contributes to chronic functional deficits after spinal cord injury. Activator and repressor screening of embryonic cortical neurons and retinal ganglion cells *in vitro* and transcriptional profiling of developing CNS neurons harvested *in vivo* have identified several candidates that stimulate robust axon growth *in vitro* and *in vivo*. Building on these studies, we sought to identify novel axon growth activators induced in the complex adult CNS environment *in vivo*. We transcriptionally profiled intact sprouting adult corticospinal neurons (CSNs) after contralateral pyramidotomy (PyX) in nogo receptor-1 knock-out mice and found that intact CSNs were enriched in genes in the 3-phosphoinositide degradation pathway, including six 5-phosphatases. We explored whether inositol polyphosphate-5-phosphatase K (*Inpp5k*) could enhance corticospinal tract (CST) axon growth in preclinical models of acute and chronic CNS trauma. Overexpression of *Inpp5k* in intact adult CSNs in male and female mice enhanced the sprouting of intact CST terminals after PyX and cortical stroke and sprouting of CST axons after acute and chronic severe thoracic spinal contusion. We show that *Inpp5k* stimulates axon growth in part by elevating the density of active cofilin in labile growth cones, thus stimulating actin polymerization and enhancing microtubule protrusion into distal filopodia. We identify *Inpp5k* as a novel CST growth activator capable of driving compensatory axon growth in multiple complex CNS injury environments and underscores the veracity of using *in vivo* transcriptional screening to identify the next generation of cell-autonomous factors capable of repairing the damaged CNS.

Key words: **CNS trauma; plasticity; regeneration; spinal cord injury; stroke; transcriptional screening**

Significance Statement

Neurologic recovery is limited after spinal cord injury as CNS neurons are incapable of self-repair post-trauma. *In vitro* screening strategies exploit the intrinsically high growth capacity of embryonic CNS neurons to identify novel axon growth activators. While promising candidates have been shown to stimulate axon growth *in vivo*, concomitant functional recovery remains incomplete. We identified *Inpp5k* as a novel axon growth activator using transcriptional profiling of intact adult corticospinal tract (CST) neurons that had initiated a growth response after pyramidotomy in plasticity sensitized nogo receptor-1-null mice. Here, we show that *Inpp5k* overexpression can stimulate CST axon growth after pyramidotomy, stroke, and acute and chronic contusion injuries. These data support *in vivo* screening approaches to identify novel axon growth activators.

Introduction

Spinal cord injury (SCI) results in chronic and debilitating deficits in sensory, motor, and autonomic function. Injured adult CNS neurons fail to regenerate because of a combination of their derisory growth potential (Curcio and Bradke, 2018) and the axon growth inhibitory environment (Schwab and Strittmatter, 2014; Bradbury and Burnside, 2019). Overcoming both impediments is critical to realizing significant functional recovery. Anti-inhibitory strategies targeting CNS myelin and chondroitin sulfate proteoglycan-enriched extracellular matrix elevate functional recovery after SCI in rodents and nonhuman primates (Freund et al., 2007; Rosenzweig et al., 2019; Wang et al., 2020) and have entered clinical trials (Kucher et al., 2018). However, interventions that target the intrinsic growth potential of damaged and intact CNS neurons, while capable of stimulating robust axon growth, have yet to reach the threshold for clinical translation.

Received Apr. 27, 2021; revised Jan. 13, 2022; accepted Jan. 14, 2022.

Author contributions: S.D.K., K.L.F., E.H.F.L., B.P.E., N.G., and W.B.J.C. designed research; S.D.K., K.L.F., E.H.F.L., B.P.E., N.G., and W.B.J.C. performed research; S.D.K., K.L.F., E.H.F.L., B.P.E., N.G., and W.B.J.C. analyzed data; S.D.K., N.G., and W.B.J.C. wrote the paper.

This work was supported by CT Bioinnovations Grant 15-RMB-Yale-02, Craig H. Neilsen Foundation Grant 340911, and National Institutes of Health | National Institute of Neurological Disorders and Stroke Grant R01-NS-095930-01.

The authors declare no competing financial interests.

Correspondence should be addressed to William B. J. Cafferty at william.cafferty@yale.edu.

https://doi.org/10.1523/JNEUROSCI.0897-21.2022

Approaches to identify growth modulators include screening the efficacy of developmentally regulated genes (Blackmore et al., 2010), phosphatases (Zou et al., 2015), kinases (Buchser et al., 2010), and genome-wide siRNA libraries (Sekine et al., 2018) to stimulate or repress neurite outgrowth in dissociated embryonic neurons *in vitro*. Additional approaches use transcriptional profiling of CNS neurons harvested *in vivo* during postnatal development (Wang et al., 2007; Moore et al., 2009; Venkatesh et al., 2018, 2021), or during injury-induced axon growth (Fink et al., 2017; Tran et al., 2019; Lindborg et al., 2021). Together, these approaches have identified *Klf6*, *Nr5a2*, *sac2*, *Lppr1* and *Rab27b*, *Myl10*, *Airn*, *Prg2*, and *Il-22*, which stimulate axon growth *in vitro* and *in vivo*. Building on *in vivo* profiling approaches, we sought to identify factors that drive intact adult corticospinal neuron (CSN) axon growth after pyramidotomy (PyX). By harvesting neurons from adult mice during periods of axon growth that support behavioral recovery, we captured a detailed snapshot of the molecular mechanisms underlying axon growth within the complex CNS environment. We used spinal retrograde tracing in μ-crystallin-GFP transgenic mice (Fink et al., 2015) and RNA sequencing to profile intact sprouting CSNs after PyX in adult nogo receptor-1 (*ngr1*) knock-out mice (Fink et al., 2017). Biological processes consistent with axon growth, guidance, and synaptogenesis were enriched in sprouting CSNs, mechanisms required for new circuit formation and integration. We found that the Hippo, mammalian target of rapamycin (mTOR), 3-phospoinositide degradation (3-PID), and lysophosphatidic acid receptor-1 (*Lpar1*) signaling pathways were enriched in sprouting neurons. We validated the axon growth-stimulating capacity of members from these pathways *in vitro* and the efficacy of targeting the LPAR1–LPPR1 signaling axis to drive the growth of intact CSN axons *in vivo* after PyX. This was the first study to probe the plasticity transcriptome and revealed a set of novel adult pro-axon growth activators. Here, we explored whether inositol polyphosphate-5-phosphatase (*Inpp5k*) could stimulate axon growth of CSNs in preclinical models of CNS trauma, including stroke and acute and chronic spinal contusion injuries.

Inpp5k is one of six 5-phosphatases enriched in intact sprouting CSNs after PyX including *Inpp5e*, *Inpp5j*, *Ocrl*, *Sac3*, and *Synj1*, highlighting a potentially important role for this family of enzymes in supporting axonal remodeling after injury. The 10 mammalian 5-phosphatases have myriad roles that include regulating protein trafficking, phagocytosis, synaptic vesicle recycling, and neuronal polarity (Ooms et al., 2009). Together, they terminate phosphoinositide-3-kinase (PI3K) signaling by converting PI(3,4,5)P3 → PI(3,4)P2. PI3K signaling has an established role in regulating actin cytoskeletal dynamics, implicating *Inpp5k* as a novel pro-axon growth activator (Zhang et al., 2018).

Here we show that overexpression of *Inpp5k* in intact CSNs significantly elevates growth of intact corticospinal tract (CST) axons after PyX and cortical stroke, and stimulates the sprouting of CST axons in the cervical spinal cord after acute and chronic severe thoracic spinal contusion injury. *In vitro* analysis revealed that *Inpp5k* enhances axon growth by releasing plasma membrane-bound cofilin, thus stimulating actin polymerization in labile axonal growth cones (GCs). These findings validate *in vivo* screening approaches to identify novel cell-autonomous axon growth activators and set the stage for additional spatial and temporal analyses to identify cell type-specific therapeutic interventions.

Materials and Methods

Mice

C57BL/6 male and female mice for tissue culture and *in vivo* experiments were ordered from The Jackson Laboratory. To minimize the number of animals used while maintaining enough rigor to achieve our scientific objectives (Festing and Altman, 2002), we used freely available power analysis (Hedwig.mgh.harvard.edu/sample_size/js/js_parallel_quant.html) to estimate sample sizes. The experiments are powered at 90% based on the number of animals in each group, the SD as determined by our previous PyX data for PyX and stroke experiments (Cafferty and Strittmatter, 2006) and BMS data for the contusion experiments (Cafferty et al., 2010), and a significance level of 0.05.

Surgery

All procedures and postoperative care were performed in accordance with the guidelines of the Institutional Animal Use and Care Committee at Yale University.

Cortical adeno-associated virus infusion

Before surgery, AAV-*Inpp5k*-V5 + AAV-mCherry or AAV-Flex-GFP + AAV-mCherry were mixed, such that the final concentration of each virus was 2.55×10^{13} viral particles/ml and aliquoted to a surgeon blind to treatment. For the PyX, stroke and acute contusion cohorts postnatal day 54 (P54) to P56 mice received unilateral infusion of adeno-associated viruses (AAVs) into primary motor cortex (M1). AAV transduction of CSNs was completed as previously described (Fink et al., 2017). Briefly, mice were anesthetized with ketamine (100 mg/kg; Covetrus) and xylazine (15 mg/kg; Covetrus). Burr holes were made over sensorimotor cortex using a dental drill, and five microinfusions of 150 nl of a 1:1 viral mixture were made to a depth of 0.7 mm (coordinates, +1 to −1 mm posterior to bregma; 0.5–1.5 mm lateral to bregma) using a Hamilton syringe and a Micro4 infusion device (World Precision Instruments) to deliver a total volume of 375 nl of each virus (total, 750 nl). All animals received postsurgical antibiotics (100 mg/kg, s.c.; ampicillin, AuroMedics) and analgesia (0.05 mg/kg s.c.; buprenorphine, Covetrus) for 2 d postlesion. Two weeks after cortical infusion, mice underwent unilateral PyX, unilateral stroke, bilateral contusion, or sham lesions (see below). For the chronic contusion cohort, mice underwent lesions at P56, and subsequent cortical infusion of AAVs 28 d later, at P84. Twenty-eight days post-PyX and stroke, 52 d post-acute contusion, and 91 d post-chronic contusion, mice were perfused with 4% paraformaldehyde (PFA; Millipore Sigma), brain and spinal cord were dissected and postfixed overnight at 4°C, and embedded in 10% gelatin (Millipore Sigma) for subsequent immunohistochemical analysis.

Unilateral PyX

Adult C57BL/6 mice ($n = 30$) were anesthetized with ketamine (100 mg/kg; Covetrus) and xylazine (15 mg/kg; Covetrus) and were placed in a supine position; an incision was made to the left of the trachea, and blunt dissection exposed the occipital bone at the base of the skull. The occipital bone was removed on the left side of the basilar artery with blunt Dumont #2 forceps to expose the medullary pyramids. The dura mater was pierced with a 30 gauge needle and resected. The left pyramid was transected with fine Dumont #5 forceps to a depth of 0.25 mm ($n = 18$) or exposed and left intact for sham lesion ($n = 12$). No internal sutures were made, and skin was closed with monofilament suture. All mice received postsurgical antibiotics (ampicillin, 100 mg/kg, s.c.) and analgesia (buprenorphine, 0.05 mg/kg, s.c.) for 2 d postlesion. One mouse from the PyX group died under anesthesia; all other mice recovered uneventfully.

Unilateral stroke

Cortical stroke was induced photochemically by modifying procedures previously described (Labat-gest and Tomasi, 2013). Adult C57BL/6 mice ($n = 35$) were anesthetized with ketamine (100 mg/kg; Covetrus) and xylazine (15 mg/kg; Covetrus), and 200 μl of 20 mg/ml Rose Bengal dye (4,5,6,7-tetrachloro-2′,4′,5′,7′-tetraiodofluorescein sodium salt; catalog #330000, Millipore Sigma) in PBS was injected intraperitoneally. Mice were then positioned in a stereotaxic frame, and a midline incision

was made in the scalp exposing the left sensorimotor cortex. The periosteum over the skull was removed, and a cold light source with a 4.5 mm aperture was centered 1 mm anterior and 0.5 mm lateral to bregma. Five minutes after Rose Bengal injection, mice were illuminated for 15 min through the intact skull to induce a cortical stroke lesion ($n = 20$) or for placement of the light source without illumination (control, $n = 15$) for sham lesion. The scalp was closed with monofilament suture. Mice received antibiotics and analgesia as above. Two mice from the control group died under anesthesia; all other mice recovered uneventfully.

Severe contusion

Adult C57BL/6 mice ($n = 52$) were anesthetized with ketamine (100 mg/kg; Covetrus) and xylazine (15 mg/kg; Covetrus). A skin incision was made along the midline of the back and thoracic vertebrae exposed via blunt muscle dissection. Laminectomy of the ninth thoracic vertebra (T9; spinal segmental level T11) was completed, and the vertebral column was stabilized using Adson forceps to grasp the lateral edges of the rostral (T7) and caudal (T10) vertebral body at the exposed foramen. The contusion probe was positioned 2 mm above the exposed T11 (Harrison et al., 2013) spinal cord, and a 75 kilodyne (kdyn) impact force was delivered to the midline of the exposed spinal cord using an Infinite Horizon impactor (Precision Systems Instrumentation), causing a severe bilateral contusion injury. Animals in the sham condition received laminectomy without impact. Animals received an internal suture of the muscle layer and external sutures before being returned to their home cage, which was placed on a heating pad. All animals received postsurgical antibiotics (ampicillin, 100 mg/kg, s.c.) and analgesia (buprenorphine, 0.05 mg/kg, s.c.) for 2 d postlesion. One mouse in the sham group and two mice in the contusion group did not recover from anesthesia, all other mice recovered uneventfully.

Histology and immunohistochemistry

Mice were killed with CO_2 and transcardially perfused with 0.9% NaCl (normal saline) with 10 U/ml heparin (1000 U/ml; Covetrus) followed by 4% PFA in PBS. Brains and spinal cords were dissected, postfixed in 4% PFA overnight at 4°C, and subsequently embedded in 10% gelatin dissolved in water for vibratome sectioning. Transverse sections (35 μm) of cervical spinal cord (C6 to C7), coronal sections of brain and brainstem, and horizontal sections of thoracic levels (contused mice) were processed for mCherry immunohistochemistry with tyramide signal amplification (catalog #NEL749A001KT, PerkinElmer). Immunofluorescence used primary antibodies directed against mCherry (1:500,000; catalog #ab205402, Abcam), V5 (1:500; catalog #V8137, Millipore Sigma), GFAP (1:2000; catalog #GA524, Agilent DAKO), and PKCγ (1:250; catalog #C19, Santa Cruz Biotechnology), and detected with secondary antibodies Alexa Fluor-488, -568, and -647 (1:500; Thermo Fisher Scientific). An investigator blinded to treatment and lesion completed all immunohistochemical procedures.

Cortical neuron cultures

Neuron dissociation. Embryonic cortical neurons were cultured as described previously (Fink et al., 2017). Briefly, embryonic day 17 (E17) mouse embryos were dissected from timed-pregnant C57BL/6 mice, and cortices were rapidly dissected in ice-cold Hibernate E medium (catalog #HECAMG, Brain Bits). Cortices were then digested for 30 min at 37°C using a digestion medium containing papain (25 U/ml; catalog #LS003126, Worthington Biochemical), DNase I (2000 U/ml; catalog #04536282001, Roche), 2.5 mM EDTA, and 1.5 mM CaCl2 in a neuronal culture medium composed of Neurobasal A (catalog #21103049, Thermo Fisher Scientific) with B27 supplement (catalog #17504044, Thermo Fisher Scientific), 1% sodium pyruvate (catalog #11360070, Thermo Fisher Scientific), 1% GlutaMAX (catalog #35050061, Thermo Fisher Scientific), and 1% Pen-Strep (catalog #P4333, Thermo Fisher Scientific). After digestion, cortices were washed twice with the neuronal culture medium and triturated in 2 ml of medium. Triturated cells were passed through a 40 μm cell strainer (Corning) and counted.

Acute dissociated cultures for outgrowth assay. Dissociated cortical neurons were electroporated with AAV plasmid vectors to overexpress a candidate gene or reporter control (either pMAX GFP or *Inpp5k*). Dissociated cortical neurons were added to 100 μl of Nucleofector solution (catalog #VPG1001, Lonza) and 3 μg of plasmid DNA. Cell mixture was transferred to a cuvette and electroporated in a Lonza Nucleofector 2b device using the preloaded device mouse hippocampal neuron electroporation parameters. Electroporated neurons were then transferred to prewarmed neuronal media and plated at a density of 2000 cells/well in an eight-well glass Lab-Tek slide (catalog #70379–82, Thermo Fisher Scientific) precoated with poly-D-lysine (catalog #P7405, Sigma-Aldrich) and laminin (catalog #L2020, Sigma-Aldrich). For neuronal outgrowth assay, neurons were cultured for 4 d at 37°C before fixation with 4% PFA in 4% sucrose.

Scrape assay. Cells were plated on 96-well plates precoated with poly-D-lysine (Corning) at a density of 50,000 cells/well in 200 µl of neuronal culture medium as described previously (Zou et al., 2015; Fink et al., 2017). Immediately after plating, 1 µl of AAV was applied to each well at a titer of 1.0×10^{10} viral particles/ml. Each plate contained wells that were treated with control AAV-YFP or AAV-mCherry virus to serve as a viral overexpression control. Neurons were then incubated at 37°C/5% CO_2. On day in vitro 7 (DIV7) and DIV14, 100 µl of medium was removed from each well and replaced with 100 µl of fresh neuronal culture medium. Before medium exchange on DIV14, 96-well cultures were scraped using a custom-fabricated 96-pin array, as described previously (Huebner et al., 2011; Fink et al., 2017). Neurons were placed back at 37°C and allowed to regenerate for 72 h before fixation with 4% PFA in 4% sucrose. Regenerating axons were then visualized by staining for βIII-tubulin (1:2000; catalog #G7121, Promega). Cell density was visualized using nuclear marker DAPI (0.2 mg/ml; Millipore Sigma) to ensure that each well contained the same number of neurons after viral treatment. Images of the center of each well were taken using a 10× objective on an ImageXpress Micro XLS High-Content Analysis System (Molecular Devices). The scrape zone was then analyzed for the total length of axons regenerating into the scrape zone in ImageJ by an investigator blind to treatment conditions. For each well, the total axon length of regenerating axons into the scrape zone was normalized to the average total axon length of regenerating axons from control wells on that individual plate to create a regeneration index. Data presented are the average regeneration index values of all wells (minimum, 27 wells/condition) from cultures obtained from three separate litters.

Immunocytochemistry. Cultures for axon growth assays and growth cone analysis were fixed with 4% PFA in 20% sucrose in PHEM buffer (300 mM PIPES, 125 mM HEPES, 50 mM EGTA, and 10 mM $MgCl_2$) for 20 min. Fixed cells were quenched with 0.1 M glycine for 15 min and permeabilized with 0.1% Triton X-100 in PBS for 5 min. Cells were washed three times in PBS then blocked at room temperature (RT) for 1 h in 2% bovine serum albumin. After blocking cells were incubated with the primary antibodies at 4°C overnight. Cells were then washed three times in PBS and incubated with secondary antibodies at RT for 2 h. Electroporated neurons were identified by visualizing the control GFP (green fluorescent protein) or by staining for the V5 (1:500; catalog #V8137, Millipore Sigma) tag on *Inpp5k*. Cells used for growth cone analyses were stained for βIII-tubulin (1:1000; catalog #G7121, Promega), phalloidin 568 conjugate (1:500; catalog #00,044, Biotum), phalloidin 405 conjugate (1:60; catalog #00034, Biotum), cofilin (1:250; catalog #ab54532, Abcam), phospho-cofilin (Ser3; 1:250; catalog #mAb3313, Cell Signaling Technology), and EB3 (1:250; catalog #ab157217, Abcam); and were detected with secondary antibodies Alexa Fluor-488 and -555 (1:500; Thermo Fisher Scientific), and Alexa Fluor-405 and -647 (1:250; Thermo Fisher Scientific).

Quantification

Cervical sections. Transverse cervical spinal cord sections were cut from all experimental animals in all experimental groups to assess $mCherry^+$ CST axon distribution in four quadrants of spinal gray matter. Images were analyzed using ImageJ software (NIH). To determine the total number of CST axons labeled per animal, images of the dorsal columns at C5 or medullary pyramid were taken at 20× on an epifluorescent microscope (Leica Microsystems) from five randomly selected sections from each animal. A 25 × 25 μm grid was then overlaid on the images, and the number of $mCherry^+$ axonal profiles in three randomly

selected boxes from the grid was counted. The average number of axons from these boxes was then scaled by the total area occupied by mCherry$^+$ axons in the dorsal column or pyramid to determine the total number of labeled axons. For axon density measurements, low-power photomicrographs of the dorsal ipsilateral (DI), dorsal contralateral (DC), ventral ipsilateral (VI), and ventral contralateral (VC) quadrants were taken at 10× to determine the area occupied by mCherry$^+$ axons. Using ImageJ, borders were drawn around the dorsal and ventral gray matter, thresholded, and skeletonized to determine the density of the area. To determine the number of midline crossing axons, sections were analyzed using Leica software to zoom. A line was drawn from the base of the dorsal columns through the ventral medial fissure. Individual mCherry$^+$ axons crossing the midline were counted. Experimenters blind to all conditions conducted the analyses. Statistical analysis was performed using Prism (GraphPad Software). Groups were analyzed using two-way ANOVA with Bonferroni's *post hoc* test for multiple comparisons between surgery and treatment groups.

Thoracic sections. Horizontal sections were cut from all contusion-lesioned mice to assess dorsal column retraction from the lesion site. Only sections where the fasciculated dorsal column was visible were included in analysis (three to five sections). Lesion size and lateral sparing were measured using the ruler feature on an epifluorescent microscope (Leica Microsystems) with software. The lesion was determined by the area surrounded by GFAP immunofluorescence. Lesion size was determined by tracing the borders enriched in GFAP immunoreactivity (IR). Lateral sparing was determined by drawing a line from the lesion edge (assessed by GFAP-IR) to the edge of the tissue. Analysis was performed by an experimenter blind to conditions. Statistics were analyzed using an unpaired two-tailed Student's *t* test to determine differences between treatment groups.

Grid walking. Experimental mice in PyX and stroke experiments underwent testing for skilled motor function using the grid walking task (Starkey et al., 2005). Mice were placed on an elevated 45 × 45 cm metal grid with 2.5 × 2.5 cm squares with dark cardboard walls creating a perimeter to make the environment more comfortable for the animals. Mice were videotaped via reflection from an angled mirror placed under the grid. Mice were recorded and allowed to explore the grid for 3 min. An experimenter blinded to treatment and lesion scored videos for the percentage of impaired steps of the first 50 steps taken for each limb. Impaired steps included a foot slip where the limb fell completely between the rungs or an incorrectly placed step where either the ankle or the tips of the digits were placed on the rung instead of proper grasping of the rung. Animals were acclimated to the grid and then tested the day before AAV infusion, the day before PyX and stroke, and on days 3, 7, 14, 21, and 28 postlesional processing. Data are presented as the average missed steps + SEM for both the impaired forelimb and hindlimb. Data were analyzed via repeated-measures ANOVA with Bonferroni's *post hoc* test for multiple comparisons of between subjects (surgery condition and treatment) and within subjects (day postinjury).

Basso mouse scale. Mice that underwent contusion and sham lesions were assessed using the Basso mouse scale (BMS; Basso et al., 2006). Two investigators blinded to treatments completed BMS scoring. Acute contusion mice received BMS scores the day before contusion, and on days 3, 7, 14, 21, 28, 35, 42, 49, and 56. Chronic contusion mice received BMS scores the day before contusion and on days 3, 7, 14, 21, 28, 35, 42, 49, 56, 63, 70, 77, 84, and 91. Data are presented as the average BMS + SEM. Data were analyzed via repeated-measures ANOVA with Bonferroni *post hoc* test for multiple comparisons of between subjects (surgery condition and treatment) and within subjects (day postinjury).

Cell culture experiments. All analyses were performed by an experimenter blinded to conditions. Slides used for axon length experiment were imaged at 20× using an epifluorescent microscope (Leica Microsystems). Five images from three different wells from 3 independant culture experiments were taken of individual neurons expressing GFP or Inpp5k-V5. The length of the longest axon (from soma to tip of axon) was measured using the Simple Neurite Tracer ImageJ plugin. Data were analyzed using an unpaired two-tailed Student's *t* test. For experiments comparing looped versus extending neurons, five growth cones were counted in five wells per biological n (3). Growth cones were visualized using βIII-tubulin and phalloidin, and were categorized as looped or extending. The percentage of extending neurons was analyzed using an unpaired two-tailed Student's *t* test. For cofilin analysis, high-power 63× images were taken using a Zeiss 880 with Airyscan processing. Five images per biological n (3) were taken of three channels (cofilin, phospho-cofilin, and phalloidin). Separate channels were analyzed using ImageJ. Each channel was autothresholded, and a border was then drawn around the phalloidin and the selection was restored onto the cofilin and phospho-cofilin channels. The density for each channel was then measured. The percentage of phospho-cofilin (phospho-cofilin/phalloidin) was subtracted from the percentage of cofilin (cofilin/phalloidin) to determine the amount of active cofilin. Data were analyzed using an unpaired two-tailed Student's *t* test. For analysis of microtubules in growth cones, high-power 63× images were taken using a Zeiss 880 with Airyscan processing. Five images per biological n (3) were taken of three channels (βIII-tubulin, EB3, and phalloidin). Each channel was autothresholded, and a segmented line was traced over each filopodia from base to tip in the phalloidin channel. The selection was restored onto the βIII-tubulin and EB3 channels, and a plot profile was acquired for each (intensity × length). Filopodia length was converted into a percentage, and the average intensity ratio of EB3/βIII-tubulin across filopodia for each growth cone was determined. Data were analyzed via repeated-measures ANOVA with Bonferroni's correction for multiple comparisons between groups (EB3/βIII-tubulin intensity) and within groups (filopodia length).

AAV production

Custom AAVs were produced as previously described (Fink et al., 2017). The AAV-mCherry construct was provided by In-Jung Kim (Yale University, New Haven, CT). This construct expresses mCherry under the CAG promoter followed by a WPRE enhancer and an SV40 polyadenylation signal. To generate AAV-CAG-mCherry, In-Jung Kim modified two AAV vectors (plasmid #18917 and #38044, Addgene). The DNA of plasmid #18917 was cut with BamHI and EcoRI, and the vector backbone was kept and ligated with mCherry insert. The mCherry sequence was amplified by PCR using the DNA of plasmid #38044 as a template with BamHI and EcoRI at the end of the amplified product for ligation.

To develop the *Inpp5k* overexpression construct, mCherry was replaced with the coding sequence of *Inpp5k* (*Inpp5k* gene ID, 19062). *Inpp5k* was PCR amplified using Platinum Pfx DNA polymerase (Thermo Fisher Scientific) from P1 brain cDNA library obtained from In-Jung Kim (forward primer, CGACCGGTCCACCATGCAGC ACGGAGACAGGAA; reverse primer, GCACCGGTGATCTGTGG CTCAGGCTCAT), we added a Kozak sequence and an Age1 restriction site to the forward primer, and an Age1 site to the reverse primer with stop codon deleted. Insertion of *Inpp5k* was completed with several steps, as follows: removal of mCherry, insertion of V5, and insertion of *Inpp5k*. mCherry was cut out of the AAV plasmid using BamHI and EcoRI, vector backbone, purified, and blunt cut (Quick Blunting Kit, Qiagen) to generate a blunted AAV vector. V5 was PCR amplified from a plasmid provided by Sourav Ghosh (Yale University; forward primer, CGGATATCACCGGTGGTAAGCCTATCCCTAAC; reverse primer, CGGATATCTCACGTAGAATCGAGACCGAG) with the forward primer containing an EcoRV and AgeI site and the reverse primer containing an EcoRV site and stop codon for V5. V5 was cut with EcoRV and ligated to blunted AAV vector. AAV-V5 and PCR-amplified candidate genes were then cut with AgeI and ligated together to generate AAV-CAG-*Inpp5k*-V5 (see Fig. 3). AAV-CAG-FLEX-EGFP-WPRE (catalog #51502, Addgene) served as a control for all *in vivo* experiments.

AAV synthesis

For AAV production, a triple-transduction method was used, as has been described previously (Park et al., 2015). Briefly, HEK293 cells were cultured in 10 15 cm plates and polyethyleneimine (Polysciences) transfected with an AAV plasmid overexpressing a candidate gene, δ F6 helper plasmid (UPenn Vector Core, University of Pennsylvania, Philadelphia, PA), and a plasmid-expressing AAV capsid 2/1 (UPenn

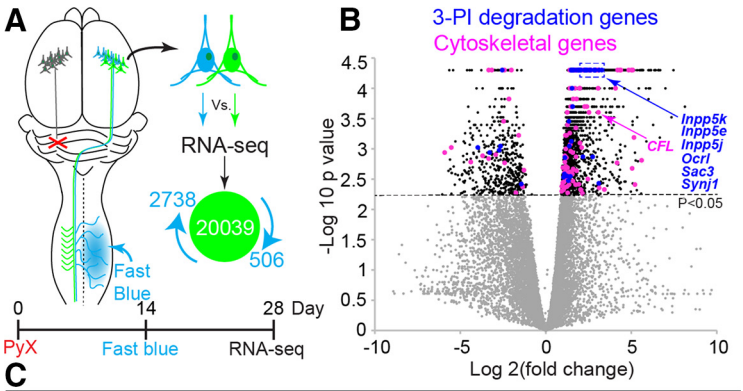

C

Canonical Pathway	Adj. P value	Diseases and Biofunctions	Adj. P value
Synaptogenesis signaling	3.89E-06	Organization of cytoplasm	3.08E-30
EIF2 Signaling	7.24E-06	Microtubule dynamics	1.73E-24
mTOR Signaling	2.34E-05	Organization of cytoskeleton	3.93E-23
AMPK Signaling	2.34E-05	Formation of cellular protrusions	7.26E-18
Reelin Signaling in Neurons	0.000123	Development of cytoplasm	3.06E-17
RAR Activation	0.000132	Development of neurons	4.08E-17
Signaling by Rho Family GTPases	0.000407	Organization of organelle	5.55E-15
Superpathway of Inositol Phosphate Compounds	0.000437	Neuritogenesis	5.73E-14
RhoGDI Signaling	0.000759	Growth of neurites	1.85E-13
Rac Signaling	0.000813	Proliferation of neuronal cells	5.04E-12
3-phosphoinositide Biosynthesis	0.001096	Outgrowth of neurons	2.03E-11
Axonal Guidance Signaling	0.001202	Branching of cells	6.22E-11
Semaphorin Neuronal Repulsive Signaling Pathway	0.001862	Outgrowth of neurites	1.18E-10
NGF Signaling	0.002138	Sprouting	1.6E-10
Actin cytoskeleton Signaling	0.004786	Formation of cytoskeleton	3.02E-10
Semaphorin Signaling in Neurons	0.005754	Morphology of cellular protrusions	4.07E-09
3-phosphoinositide Degradation	0.00631	Branching of neurons	2.57E-08
Ephrin B Signaling	0.007943	Dendritic growth/branching	5.78E-08
PTEN Signaling	0.007943	Branching of neurites	8.06E-08
D-myo-inositol 4-Phosphate Biosynthesis	0.008128	Organization of cellular membrane	8.41E-08

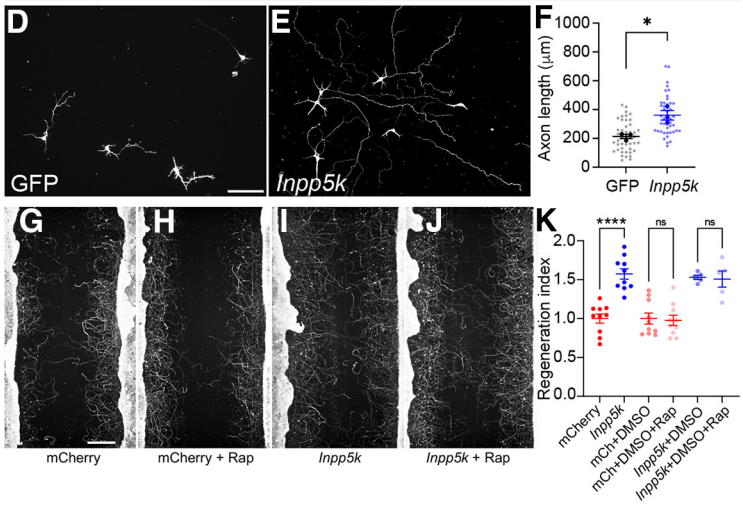

Figure 1. *Inpp5k* enhances neurite outgrowth and regeneration *in vitro*. ***A***, Schematic shows the approach to identify intact CSNs undergoing axon growth after PyX. Adult *ngr1*$^{+/+}$ *crym*-GFP and *ngr1*$^{-/-}$ *crym*-GFP transgenic mice received a PyX, 14-d-postlesion mice received a contralateral infusion of the retrograde tracer Fast Blue, and 28-d-postlesion mice were prepared for laser capture microdissection of intact quiescent CSNs (GFP$^+$/FB$^-$) and intact sprouting CSNs (GFP$^+$/FB$^+$; Fink et al., 2017). Differential gene expression analysis, calculated using a Wilcoxon rank-sum test, showed that 2738 genes were significantly upregulated and 506 genes were downregulated in sprouting versus quiescent CSNs. ***B***, Volcano plot shows every gene profiled as log2-fold change versus –log10 of the false discovery rate (FDR)-corrected *p* value. Non-SDE genes (gray dots) are separated from SDE genes (black dots) by $p < 0.05$ cutoff (stippled) line. Inositol phosphate genes (dark blue) and genes associated with the cytoskeleton (magenta dots) are primarily enriched in sprouting CSNs. Six 5-phosphatases (*Inpp5k*, *Inppe5*, *Inpp5j*, *Ocrl*, *Sac3*, *Synj1*) and cofilin (CFL) are highlighted. IPA was conducted on genes enriched in sprouting CSNs. ***C***, Table shows the IPA output of significantly upregulated "Canonical Pathways" and "Diseases and Biofunctions" across the whole dataset of differentially expressed genes (with Benjamini–Hochberg corrected *p* values for multiple comparisons), and canonical pathways associated with inositol phosphate signaling are highlighted in blue, and cytoskeletal dynamics in magenta. ***D–F***, Dissociated E17.5 cortical neurons overexpressing *Inpp5k*-V5 (***E***), showed significant longer neurites compared with GFP controls (***D***, ***F***; average total axon length of GFP ($n = 45$, gray dots) and *Inpp5k*-V5 ($n = 45$, light blue dots) neurons from $n = 3$ independent experiments ($t_{(4)} = 4.066$, $^*p = 0.015$, unpaired two-tailed *t* test) after DIV4. Data shown are the mean length of axon (in micrometers; biological n, darker dots) ± SEM. ***G–J***, To assess whether *Inpp5k*-mediated enhanced neurite growth was mTOR dependent, we transduced E17.5 cortical neurons with AAV-mCherry or AAV-*Inpp5k*+/−300 nM rapamycin in Vector Core). Cells were harvested, pelleted, and resuspended in freezing buffer (0.15 M NaCl and 50 mM Tris, pH 8.0) 48–60 h after transfection. For viral purification, cells were lysed by undergoing two freeze–thaw cycles followed by benzonase treatment (EMD Chemical) for 30 min at 37°C. Lysate supernatant was collected by spinning tubes in a swinging bucket rotor (Eppendorf) at 3700 × *g* for 20 min. Lysate supernatant was then added dropwise to the top of a centrifuge tube containing a 15, 25, 40, and 60% iodixanol step gradient. The gradient was spun in a Vti50 rotor (Beckman Coulter) at 50,000 rpm for 2 h at 10°C. The 40% fraction was collected and added to an Amicon Ultracel 100K (Millipore) for buffer exchange to PBS. A small amount of virus was used to test viral titer using quantitative PCR. Concentration of virus was repeated on smaller Amicon Ultracels (Millipore) until the desired high titer was reached. Final purified virus was aliquoted and stored at −80°C.

Results

Inositol phosphate compounds are enriched in intact sprouting CSNs after contralateral PyX

In a recent study, we completed transcriptional profiling of intact sprouting CSNs after contralateral PyX (Fig. 1*A*) in plasticity-sensitized nogo receptor-1 knock-out mice (*ngr1*$^{-/-}$). Using laser capture microdissection 28 d after unilateral PyX and 14 d after contralateral intraspinal injection of fast blue (FB) in *crym*-GFP transgenic mice, we completed bulk RNA sequencing of intact nonsprouting CSNs (GFP$^+$/FB$^-$) and intact sprouting CSNs (GFP$^+$/FB$^+$). Differential gene expression analysis revealed that 2738 genes were upregulated and 506 were downregulated in intact sprouting versus nonsprouting CSNs (Fig. 1*A*). To gain biological insight into the functions of these significantly differentially expressed (SDE) genes, we used ingenuity pathway analysis (IPA). As reported in our previous study (Fink et al., 2017), pathways consistent with actin cytoskeletal dynamics, axon growth, axon guidance, and synaptogenesis were found to be significantly dysregulated in intact sprouting CSNs after PyX (Fig. 1*B*,*C*). Additionally, we found that several pathways associated with inositol phosphate signaling were also dysregulated; specifically, we found that six 5-phosphatases in the 3-PID pathway were

←

DMSO. ***K***, Neurons expressing mCherry showed minimal regeneration into the scrapped zone, while *Inpp5k*-expressing neurons showed a significant increase in regeneration compared with control. There was no significant difference in the neurite regeneration on addition of rapamycin to mCherry or *Inpp5k*-treated neurons (one-way ANOVA, using *post hoc* Tukey's HSD test: $^{****}p < 0.0001$, $F_{(5,44)} = 18.24$). Scale bars: ***D***, 100 μm; ***H***, 200 μm.

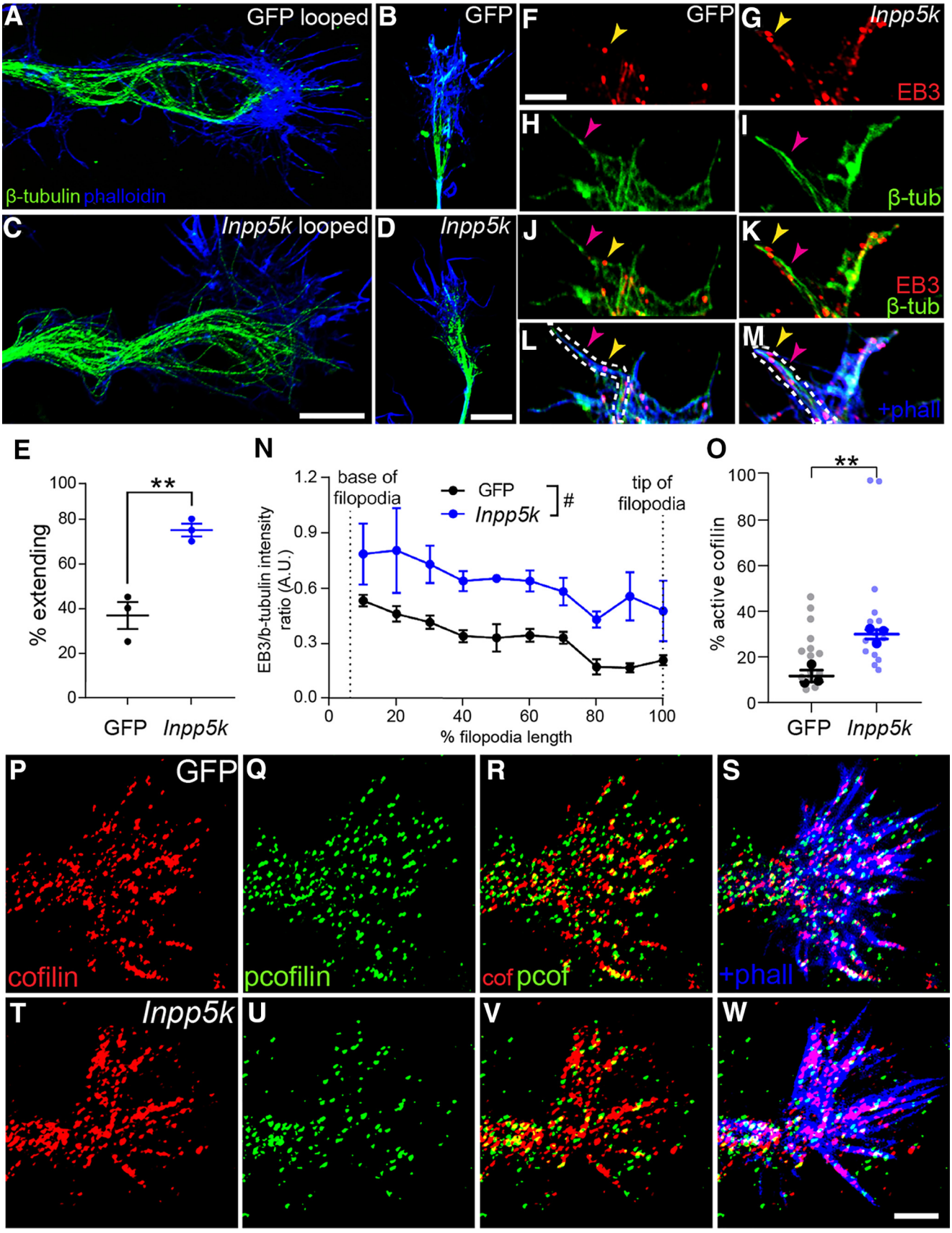

Figure 2. *Inpp5k* increases active cofilin and microtubule advancement in growth cones *in vitro*. ***A–D***, Assessment of the morphology of GCs of E17.5 cortical neurons transduced with GFP (***A***, ***B***) and *Inpp5k* (***C***, ***D***). ***E***, At DIV4, β-tubulin (green) and phalloidin (blue) labeling showed that significantly more GCs with extending versus looped morphology in *Inpp5k*-treated cultures compared with controls [GFP ($n = 60$) and *Inpp5k*-V5 ($n = 60$) neurons from $n = 3$ independent experiments; unpaired two-tailed t test: $t_{(4)} = 5.75$, $^{**}p = 0.005$, data are shown as the mean percentage of extending growth cones $\pm$ SEM]. ***F–N***, Assessment of the relative filopodial location and density of $EB3^{+}$ comets in GCs of E17.5 cortical neurons transduced with GFP (***F***, ***H***, ***J***,

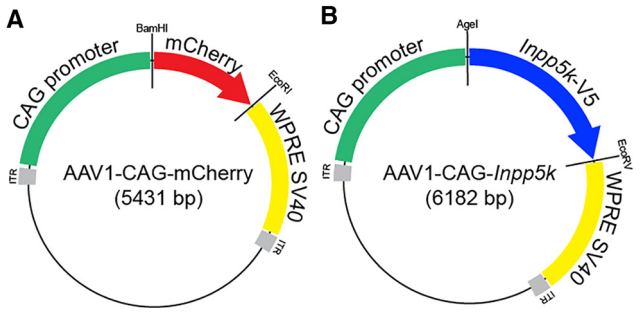

Figure 3. Plasmid maps for *in vivo* transduction of CSNs. ***A***, ***B***, Plasmid map shows AAV1-CAG-mCherry (***A***) and AAV1-CAG-*Inpp5k-V5* (***B***) and the restriction sites used for subcloning for adeno-associated viral vector constructs for transduction of corticospinal neurons *in vivo* (for comprehensive cloning strategy, see Materials and Methods).

among the most highly enriched genes in intact sprouting CSNs (Fig. 1*B*), including *Inpp5e*, *Inpp5j*, *Inpp5k*, *Ocrl*, *SacIII*, and *Synj1*. IPA also revealed that cytoskeletal functions were the most enriched disease and biofunction terms within our SDE gene set (Fig. 1*C*). These data suggest that inositol signaling is converging with the cytoskeleton in intact sprouting CSNs after contralateral PyX and thus form part of the molecular machinery driving axon growth in these neurons. We selected *Inpp5k* to probe the possible impact of the 3-PID pathway to stimulate axon growth *in vitro* and *in vivo*. To explore, we transfected dissociated E17.5 cortical neurons with vectors encoding either GFP or V5-tagged *Inpp5k*. After DIV4, neurons were fixed and stained with antibodies against GFP, βIII-tubulin, and V5. Neurons transfected with *Inpp5k* grew significantly longer neurites compared with GFP controls (Fig. 1*D–F*). These data are consistent with our previous finding showing that *Inpp5k* enhances axon growth of acutely dissociated cortical neurons at DIV3 (Fink et al., 2017). To explore whether *Inpp5k* was enhancing neurite outgrowth via mTOR, we completed the *in vitro* scrape assay (Zou et al., 2015; Fink et al., 2017; Sekine et al., 2018), including the mTORC1 inhibitor rapamycin in culture media after the *in vitro* injury. Neurons transfected with *Inpp5k* showed significantly more neurite growth into the scrapped area compared with mCherry-transfected controls (Fig. 1*G–K*). Inclusion of DMSO (rapamycin diluent) ± 300 nM rapamycin did not impact neurite growth of cells transfected with either mCherry or *Inpp5k*. These data show that *Inpp5k* is stimulating enhanced axon growth *in vitro* via an mTOR-independent mechanism.

←

L; EB3, red; β-tubulin, green; phalloidin, blue; pink arrows show colocalized EB3$^+$ comets and microtubules; dotted line indicates the border of filopodia) and *Inpp5k* (***G***, ***I***, ***K***, ***M***) shows that *Inpp5k* significantly elevated the density of EB3$^+$ comets along filopodia (***N***; $F_{(1,4)} = 10.21$, $p = 0.033$, two-way ANOVA with repeated measures with Bonferroni's *post hoc* comparisons), and the distance to which EB$^+$ comets were found in distal regions of filopodia ($F_{(1.339,5.356)} = 6.722$, $p = 0408$, two-way ANOVA with repeated measures with Bonferroni's *post hoc* comparisons). Data shown are EB3/β-tubulin intensity across the percentage of filopodia length ± SEM. ***O–W***, Assessment of the relative density of (active) cofilin (red) and (inactive) phospho-cofilin (green) in GCs of E17.5 cortical neurons after DIV4 transduced with GFP (***P–S***) and *Inpp5k* (***T–W***) shows that *Inpp5k*-treated cultures had significantly more active cofilin compared with controls (***O***; unpaired two-tailed *t* test, $t_{(4)} = 5.531$, $^{**}p = 0.005$). Data shown are the mean density of active cofilin (biological n, darker dots; lighter dots, GCs; $n = 15$/condition) ± SEM. Scale bars: ***C***, 20 μm; ***D***, 10 μm; ***F***, 4 μm; ***W***, 4 μm.

Inpp5k increases active cofilin and microtubule advancement in growth cones *in vitro*

SDE genes in intact sprouting CSNs were enriched in pathways consistent with cytoskeletal rearrangements (Fig. 1*C*). To explore whether *Inpp5k* was resculpting the axonal cytoskeleton and enhancing neurite growth, we assessed the morphology of E17.5 cortical neuron GCs transfected with *Inpp5k* or GFP at DIV4. Strikingly, *Inpp5k*-transfected neurons showed a significantly higher number of growth cones with an elongating or extending morphology compared with controls (Fig. 2*A–E*). While some GFP-transfected neurons displayed elongating GCs, the majority were in a looped or stalled growth morphology at DIV4 (Fig. 2*E*). Previous studies have shown that a loss of active cofilin (nonphosphorylated form) decreases radially oriented filopodia, slows the advancement of microtubules into the periphery of GCs, and thus increases the microtubule looping trajectories observed in stationary growth cones (Flynn et al., 2012). To explore whether *Inpp5k* was enhancing neurite growth via a similar mechanism, we examined the number of end binding protein 3 (EB3) comets extending into peripheral filopodia in *Inpp5k*- and GFP-treated cultures. Significantly more EB3$^+$ comets colocalizing with βIII-tubulin$^+$ microtubules were observed along the entire length of peripheral filopodia in *Inpp5k*-treated cultures compared with those of controls (Fig. 2*F–N*), indicating that an increased advancement of microtubules was driving the increased number of elongating growth cones after *Inpp5k* treatment. Furthermore, the density of active cofilin was increased in GCs after *Inpp5k* treatment compared with control (Fig. 2*O–W*). These data are consistent with the finding that *Inpp5k* has specificity for hydrolysis of PI(4,5)P_2 (Yonezawa et al., 1990, 1991; Ijuin et al., 2000) and that hydrolysis of PI(4,5)P_2 results in a release and activation of a membrane-bound pool of cofilin (van Rheenen et al., 2007, 2009). Together, these data suggest that the mechanism of increased axon extension in neurons overexpressing *Inpp5k* works via an increased available pool of active cofilin.

Inpp5k enhances plasticity of intact CSNs after unilateral pyramidotomy

As overexpression of *Inpp5k* increased the axon growth of cortical neurons *in vitro*, we next sought to determine whether the overexpression of *Inpp5k* could increase axon growth *in vivo* after CNS trauma. As our transcriptional screen (Fink et al., 2017) identified *Inpp5k* as enriched in intact CSNs after contralateral PyX, we initially sought to determine whether overexpression of *Inpp5k* in intact CSNs could drive sprouting of intact CST arbors. To explore, we coinfused either AAV-mCherry (Fig. 3*A*) and AAV-FLEX-GFP (control) or AAV-*Inpp5k*-V5 (Fig. 3*B*) and AAV-mCherry (Fig. 4*A*) into the right cortex of adult wild-type (C57BL/6) mice 2 weeks before unilateral PyX (Fig. 4*A*). Twenty-eight days postlesion, mice were killed and processed for histology. *Inpp5k*-V5 and mCherry are colocalized at the injection site (Fig. 4*B*,*C*) in layer 5 CSNs and in CST axons in the spinal dorsal columns (Fig. 4*D*,*E*), confirming that mCherry can be used as a marker for transduced CSNs, their axons, and their terminals.

CST axons expressing mCherry were present in the spinal dorsal and lateral columns, and throughout the gray matter contralateral to the cortical injection in transverse sections through C6/7 4 weeks after PyX (Fig. 4*F–I*). PKCγ-IR confirmed complete axotomy of CST axons in PyX-lesioned groups (Fig. 4*G*′, *I*′). Counting mCherry$^+$ puncta in the dorsal columns revealed no differences between lesions nor treatment among the groups (Fig. 4*J*), showing that *Inpp5k* did not affect the survival or health

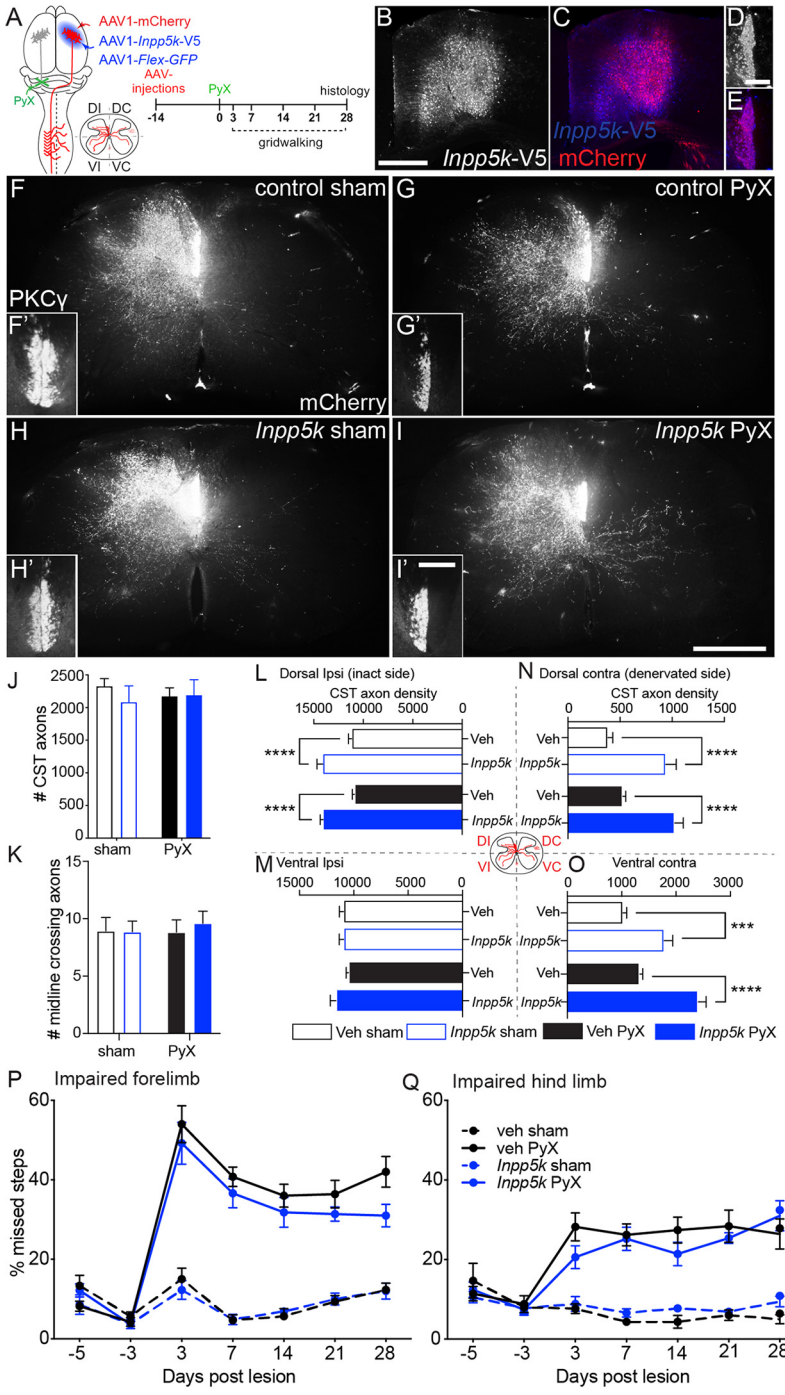

Figure 4. Inpp5k increases CST sprouting following PyX. ***A***, Schematics show relative locations of PyX and cortical injection of AAV1-mCherry and AAV1-*Inpp5k*-V5. Bottom right, Schematic of transverse cervical sections with mCherry (red) labeling in four quadrants that were analyzed; right, experimental timeline. ***B–E***, Photomicrographs show V5 (***B***, ***D***) and mCherry (***C***, ***E***) staining in M1 cortex (***B***, ***C***) and C4 spinal cord (***D***, ***E***) 42 d after AAV infusion, confirming the expression of *Inpp5k* and the reporter in CSNs and CST axons. ***F–I***, Photomicrographs show mCherry$^+$ CST axon staining in transverse sections of C6 spinal cord from mice that received AAV1-mCherry$^+$AAV1-FLEX-GFP 28 d after sham lesion (***F***) and PyX (***G***) and *Inpp5k* treatment 28 d after sham lesion (***H***) and PyX (***I***). ***F′–I′***, Insets, PKC$^\gamma$-IR in both dorsal column projections in sham-lesioned mice (***F′***, ***H′***) and intact contralateral dorsal columns after PyX (***G′***, ***I′***). ***J***, There was no significant difference in the number of CST axons traced between groups (two-way ANOVA with Bonferroni's *post hoc* comparisons, $p > 0.05$; data are shown as the average number of labeled CST axons ± SEM). ***K***, There was no significant difference in the number of mCherry$^+$ CST axons that crossed the spinal midline between groups (two-way ANOVA with Bonferroni's *post hoc* comparisons, $p > 0.05$; data are shown as the average number of labeled CST axons ± SEM). ***L***, Densitometric analysis of mCherry$^+$ CST axons in the DI quadrant showed that there was a main effect of *Inpp5k* treatment ($F_{(1,25)} = 71.78$, $p < 0.0001$, two-way ANOVA with Bonferroni's *post hoc* multiple comparisons test, $^{****}p < 0.0001$; control sham, $n = 5$; control PyX, $n = 11$; *Inpp5k* sham, $n = 6$; *Inpp5k* PyX, $n = 7$), but no effect of lesion. ***M***, There was no significant impact of lesion or treatment on CST density in the VI quadrant. ***N***, In the DC quadrant, there was a main effect of *Inpp5k* treatment ($F_{(1,25)} = 62.8$, $p < 0.0001$; two-way ANOVA with Bonferroni's *post hoc* multiple-comparisons test, $^{****}p < 0.0001$), and no effect of lesion. ***O***, In the VC quadrant, there was a main effect of *Inpp5k* treatment ($F_{(1,25)} = 67.45$, $p < 0.0001$, two-way ANOVA with Bonferroni's *post hoc* multiple-comparisons test: $^{****}p < 0.0001$, $^{***}p = 0.004$). All densitometric analysis data are shown as average mCherry$^+$ signal density ± SEM. CST function was assessed using the grid-walking apparatus. ***P***, ***Q***, No significant differences were found between *Inpp5k* PyX-treated and control PyX-treated subjects for the forelimbs (***P***; two-way ANOVA with repeated measures with Bonferroni's *post hoc* comparisons, $p > 0.05$; data shown are the average percentage of missteps ± SEM) or the hindlimbs (***Q***; two-way ANOVA with repeated measures with Bonferroni's *post hoc* comparisons test, $p > 0.05$, data shown are the average percentage of missteps ± SEM. Scale bars: ***B***, 1 mm; ***D***, 100 μm; ***I***, 500 μm; ***I′***, 100 μm.

of intact CST axons. To analyze CST sprouting on both the intact and denervated sides of the spinal cord, we partitioned the cord into the following four quadrants: DI, DC, VI, and VC (Fig. 4*A*, scheme). Here, laterality is described in reference to the lesion; therefore, as the CST crosses the midline in the medulla of the brainstem, dorsal ipsilateral refers to the dorsal quadrant innervated with intact CST axons. In the DI quadrant, *Inpp5k* overexpression significantly enhanced CST axon density after both PyX and sham lesion (Fig. 4*L*). There was no effect of lesion or treatment on CST axon density in the VI quadrant (Fig. 4*M*). *Inpp5k* overexpression significantly enhanced CST density in both the DC (Fig. 4*N*) and VC quadrants (Fig. 4*O*) after PyX and sham lesion. There was no significant interaction between lesion and treatment in any quadrant, suggesting that *Inpp5k* drives CST axon growth regardless of any lesion-induced stimuli from the surrounding microenvironment undergoing degeneration. No difference was seen in the number of mCherry$^+$ CST axons crossing the midline between groups (Fig. 4*K*), suggesting that an increase in CST density was because of the sprouting of arbors that were already present in the contralateral spinal gray matter.

To explore whether the enhanced sprouting of intact CST arbors after *Inpp5k* treatment enhanced functional recovery after contralateral PyX, CST function was assessed using an elevated grid-walking task. Neither control- nor *Inpp5k*-treated sham-lesioned mice showed a deficit in post-training ability of their forelimbs or hindlimbs to navigate the grid at any time during the testing period, confirming that *Inpp5k* was not negatively impacting the function of an entirely intact CNS (Fig. 4*P*–*Q*). However, both *Inpp5k*-treated and control-treated mice showed a significant increase in the number of missed steps 3 d after PyX, in both the forelimbs (Fig. 4*P*) and the hindlimbs (Fig. 4*Q*) on the affected side. The number of missed

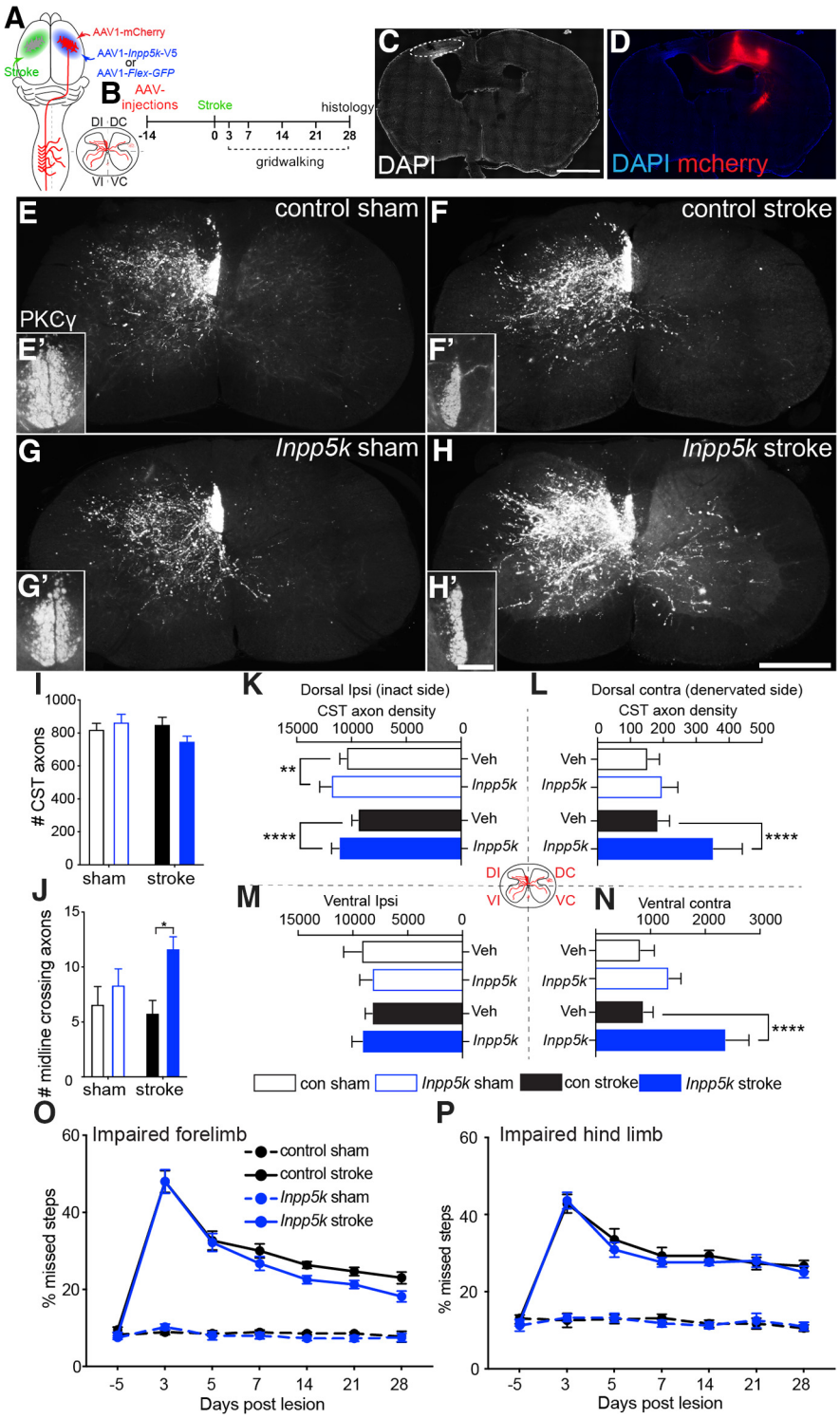

Figure 5. *Inpp5k* overexpression enhances the sprouting of intact CSNs following stroke. ***A***, Schematic shows unilateral cortical stroke (green) and delivery of AAV1 mCherry and *Inpp5k*-V5 into contralateral cortex. Inset schematic shows quadrants of cord analyzed as before. ***B***, Experimental timeline. ***C***, ***D***, Photomicrographs show the accumulation of DAPI^{+} nuclei delineating the stroke location (***C***, stippled oval) in the motor cortex and mCherry^{+} CSNs in contralateral cortex 4 weeks after lesion (***D***). ***I***, The number of mCherry^{+} CST axons counted in the C4 spinal segment was invariant between groups. ***E–H***, Photomicrographs show transverse sections through C6 showing mCherry^{+} CST axon labeling in control sham (***E***; $n = 6$), control stroke (***F***; $n = 11$), *Inpp5k* sham (***G***; $n = 7$), and *Inpp5k* stroke (***H***; $n = 9$) 4 weeks postlesion. ***E′***, ***F′***, ***G′***, ***H′***, Insets, PKC$^{\gamma}$-IR revealing complete unilateral denervation of CST in stroke subjects (***F′***, ***H′***) and intact dorsal columns in sham subjects (***E′***, ***G′***). ***K***, Densitometric analysis in the DI quadrant showed that there was a main effect of *Inpp5k* treatment ($F_{(1,29)} = 36.51$, $p < 0.0001$; two-way ANOVA with Bonferroni's *post hoc* multiple-comparisons test, $^{**}p < 0.001$, $^{****}p < 0.0001$). ***M***, There was no significant impact of lesion or treatment on CST density in the VI quadrant. ***L***, In the DC quadrant, there was a main effect of *Inpp5k* treatment ($F_{(1,29)} = 27.96$, $p < 0.0001$; two-way ANOVA with Bonferroni's *post hoc* multiple-comparisons test, $^{****}p < 0.0001$). ***N***, In the VC quadrant, there was a main effect of *Inpp5k* treatment ($F_{(1,29)} = 32.13$, $p < 0.0001$; two-way ANOVA with Bonferroni's *post hoc* multiple-comparisons test, $^{****}p < 0.0001$). All densitometric analysis data are shown as the average mCherry^{+} signal density ± SEM. ***J***, The number of midline crossing CST axons was also significantly elevated in mice treated with *Inpp5k* after stroke ($F_{(1,29)} = 9.396$, $^{\#\#}p = 0.005$; two-way ANOVA with Bonferroni's *post hoc* comparisons test). ***O***, ***P***, Assessment of CST function using grid-walking analysis revealed that there were no significant differences between *Inpp5k* stroke-treated and control stroke-treated subjects in the percentage of missed steps for forelimbs (***O***; two-way ANOVA with repeated measures with Bonferroni's *post hoc* comparisons test, $p > 0.05$) and hindlimbs (***P***; two-way ANOVA with repeated measures with Bonferroni's *post hoc* comparisons test, $p > 0.05$, data shown are the average percentage of missteps ± SEM). Scale bars: ***C***, 2 mm; ***I***, 500 μm; ***I′***, 100 μm.

steps observed by the forelimbs recovered modestly over time; however, the hindlimbs maintained a steady functional deficit throughout the testing period. There was no significant difference in recovery between *Inpp5k*-treated and control-treated mice.

Inpp5k enhances plasticity of intact CSNs following stroke

We next sought to explore whether cortical overexpression of *Inpp5k* could also stimulate the growth of intact CSNs after cortical stroke. To this end, we completed unilateral photothrombotic stroke lesions in M1 (Fig. 5*A*) in wild-type mice. Two weeks before stroke lesion, wild-type mice received unilateral (right side) cortical injections of either AAV-*Inpp5k*-V5 and AAV-mCherry or AAV-FLEX-GFP (control) and AAV-mCherry to label intact CSNs for anatomic analyses (Fig. 5*B*). Photothrombotic stroke resulted in a reproducible ischemic lesion in M1 while minimally damaging subcortical structures (Fig. 5*C*). We did not detect retrograde transduction of CSNs in ipsilateral cortex in sham-lesioned or stroke-lesioned mice after control or *Inpp5k* treatment, thereby ensuring that all anatomic tracing and behavioral outcomes 4 weeks postlesion were dependent on CSNs in the intact cortex (Fig. 5*D*). Histologic assessment of mCherry^{+} CST axons 28 d postlesion showed that a consistent number of axons were labeled in the medullary pyramids regardless of lesion and/or treatment (Fig. 5*I*). Transverse sections of cervical cord showed mCherry CST^{+} axons in one side of the dorsal columns and throughout gray matter on the intact side of the

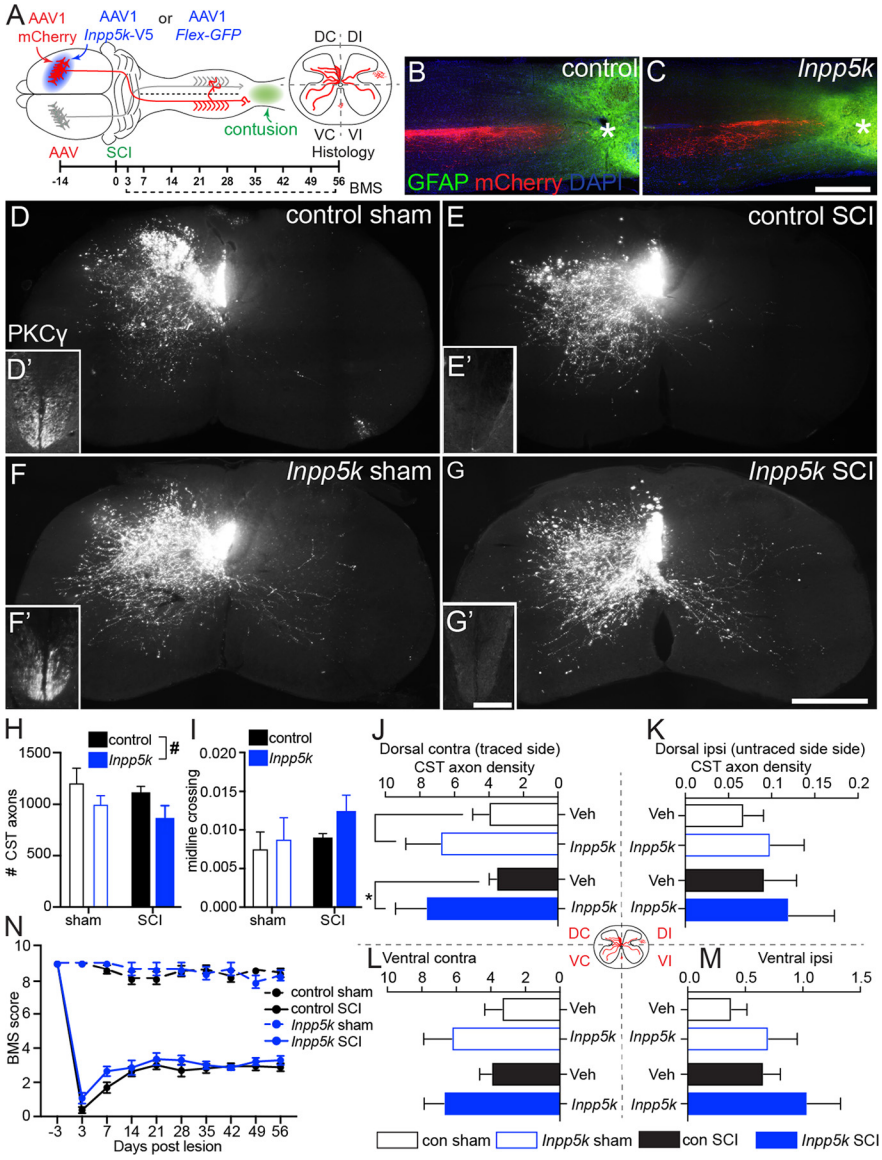

Figure 6. *Inpp5k* overexpression increases sprouting of CST axons after acute contusion injury. ***A***, Schematic shows bilateral T11 contusion injury (green) and delivery of AAV1 mCherry and *Inpp5k*-V5 into the right side of motor cortex. Inset, Schematic shows the quadrants of cord analyzed, with laterality determined via the injection side as the lesion is bilateral, so the left side of the cord for contusion experiments is labeled contralateral. Inset shows the experimental timeline. ***B***, ***C***, Photomicrographs show horizontal sections through the lesion site 4 weeks after severe contusion injury in control mice (***B***; mCherry$^+$ CST axons, red; GFAP, green; asterisks indicate lesion site) and *Inpp5k*-treated mice (***C***). No mCherry$^+$ CST axons grew into or past the lesion site. ***H***, The average number of mCherry$^+$ CST axons counted in the dorsal columns was significantly different between groups ($F_{(1,21)} = 5.215$, $p = 0.033$, two-way ANOVA with Bonferroni's *post hoc* comparisons test; data shown are the average number of mCherry$^+$ axons ± SEM); therefore, subsequent densitometric data were normalized to the number of CST axons per animal. ***D***, ***E***, ***F***, ***G***, Photomicrographs show transverse sections through C6 showing mCherry$^+$ CST axon labeling in control sham (***D***; $n = 5$), control SCI (***E***; $n = 9$), *Inpp5k* sham (***F***; $n = 4$), and *Inpp5k* SCI (***G***; $n = 7$). ***D′***, ***E′***, ***F′***, ***G′***, Insets, PKC$^\gamma$-IR revealing intact lumbar dorsal columns for sham-lesioned mice (***D′***, ***F′***), and complete absence after SCI subjects (***E′***, ***G′***). ***J***, Densitometric analysis in the DC quadrant showed that there was a main effect of *Inpp5k* treatment ($F_{(1,21)} = 6.608$, $p = 0.0178$, two-way ANOVA with Bonferroni *post hoc* multiple-comparisons test, $^*p = 0.0387$). ***L***, In the VC quadrant, there was a main effect of *Inpp5k* treatment ($F_{(1,21)} = 6.776$, $p = 0.0166$, two-way ANOVA with Bonferroni's *post hoc* multiple-comparisons test). ***K***, ***M***, There was no significant impact of lesion or treatment on CST density in the DI (***K***) or VI (***M***) quadrants. All densitometric data are shown as the average number of mCherry axons normalized compared with the number of dorsal column axons per animal ± SEM. ***I***, There was no significant difference in the number of midline crossing CST axons between lesion and treatment groups (data shown are the average number of mCherry axons normalized to the number of dorsal column axons ± SEM). ***N***, Behavioral assessment using the BMS revealed that there was no significance between *Inpp5k*-treated and control-treated SCI mice (two-way ANOVA with repeated measures with Bonferroni's *post hoc* comparisons, $p > 0.05$; data shown are the average BMS score ± SEM). Scale bars: ***C***, 2 mm; ***H***, 500 µm; ***H′***, 100 µm.

spinal cord (Fig. 5*E–H*). PKCγ-IR confirmed that the stroke was unilateral and complete in lesioned groups (Fig. 5*F′*, *H′*). As described above, we partitioned the spinal cord into four quadrants to assess the density of CST innervation in dorsal and ventral gray matter in stroke- and sham-lesioned mice. In the DI quadrant, *Inpp5k* overexpression significantly enhanced CST axon density after both stroke and sham lesion (Fig. 5*K*). There was no effect of lesion or treatment on CST density in the VI quadrant (Fig. 5*M*). *Inpp5k* overexpression significantly enhanced CST density in both the DC (Fig. 5*L*) and VC (Fig. 5*N*) quadrants after both stroke and sham lesioning. Similar to the PyX study, there was no significant interaction between lesion and treatment, further supporting the observation that a lesion-induced stimulus is not essential to the progrowth effects of *Inpp5k*. The number of CST axons crossing the spinal midline was also increased after stroke in the *Inpp5k*-treated group (Fig. 5*J*). To examine whether enhanced sprouting of CST axons contributed to functional recovery after stroke, we assessed fine motor skills using the grid-walking task. As expected, we found that stroke significantly impaired both the forelimbs and hindlimbs on the affected side compared with sham-lesioned mice (Fig. 5*O*,*P*). However, there was no significant difference in the functional recovery observed between the control and *Inpp5k*-treated groups (Fig. 5*O*,*P*).

Inpp5k increases sprouting of CST axons following acute contusion SCI

Based on our observations that *Inpp5k* increases the sprouting of intact CSNs in two models of plasticity, we wanted to determine whether *Inpp5k* overexpression could enhance regeneration of axotomized CSNs in a preclinical model of SCI, specifically in an acute and chronic severe thoracic contusion injury model. To explore, we injected either AAV-*Inpp5k*-V5 and AAV-mCherry or AAV-FLEX-GFP (control) and AAV-mCherry into the right motor cortex of adult wild-type mice 2 weeks before a 75 kdyn contusion at T11 or a sham lesion (Fig. 6*A*). Hindlimb motor function was assessed for 8 weeks using the BMS. Horizontal sections through midthoracic cord showed mCherry$^+$ CST axons regenerating up to the penumbra of the GFAP-enriched lesion site in both control (Fig. 6*B*) and *Inpp5k*-treated (Fig. 6*C*) mice. No CST axons were seen penetrating through the lesion and entering the spinal cord caudal

to the lesion site in either group. Analysis of tissue sparing around the lesion confirmed that there was no difference between groups ($t_{(1.706)} = 11$, $p = 0.116$, unpaired two-tailed t test). Furthermore, there was no significant difference in the retraction of the mCherry$^+$ CST axon regeneration front between the two groups. These data confirm that *Inpp5k* is not stimulating regeneration of axotomized CST axons directly at the lesion site.

As we had observed significant plasticity of intact CST axons after PyX and stroke lesion, we explored whether *Inpp5k* could stimulate axon sprouting in the cervical spinal cord after thoracic contusion injury. As we had treated and labeled only one side of cortex, we were able to complete similar analysis to our above PyX-lesioned and stroke-lesioned mice. As the lesion was bilateral for contusion studies, laterality was determined via injection side; therefore, the left side of the spinal cord is labeled contralateral. Transverse sections of C6/7 spinal cord show mCherry$^+$ CST axons in the left dorsal column and densely innervating one side of the spinal gray matter (Fig. 6*D–G*). PKCγ-IR was observed bilaterally in the L4 segment of spinal cord in sham-lesioned mice (Fig. 6*D′*,*F′*) and were entirely absent from L4 in mice that underwent contusion, confirming complete severing of the CST (Fig. 6*E′*,*G′*). In the DC and VC quadrants, *Inpp5k* overexpression significantly enhanced CST axon density after both contusion and sham lesion (Fig. 6*J*,*L*). There was no effect of lesion or the treatment on CST axon density in the DI or VI quadrants (Fig. 6*K*,*M*). Similar to PyX and stroke lesions, there was no significant interaction between lesion and treatment further supporting an effect of *Inpp5k* in the absence of lesion-induced stimuli. There was no difference in the number of mCherry$^+$ CST axons crossing the midline (Fig. 6*I*). Furthermore, there was no significant difference in hindlimb motor recovery between control- and *Inpp5k*-treated mice after contusion (Fig. 6*N*) using the BMS. Thus, *Inpp5k* overexpression enhances sprouting of intact or lesioned CST axons rostral to the severe contusion injury but does not stimulate the regeneration of cut axons through the lesion site.

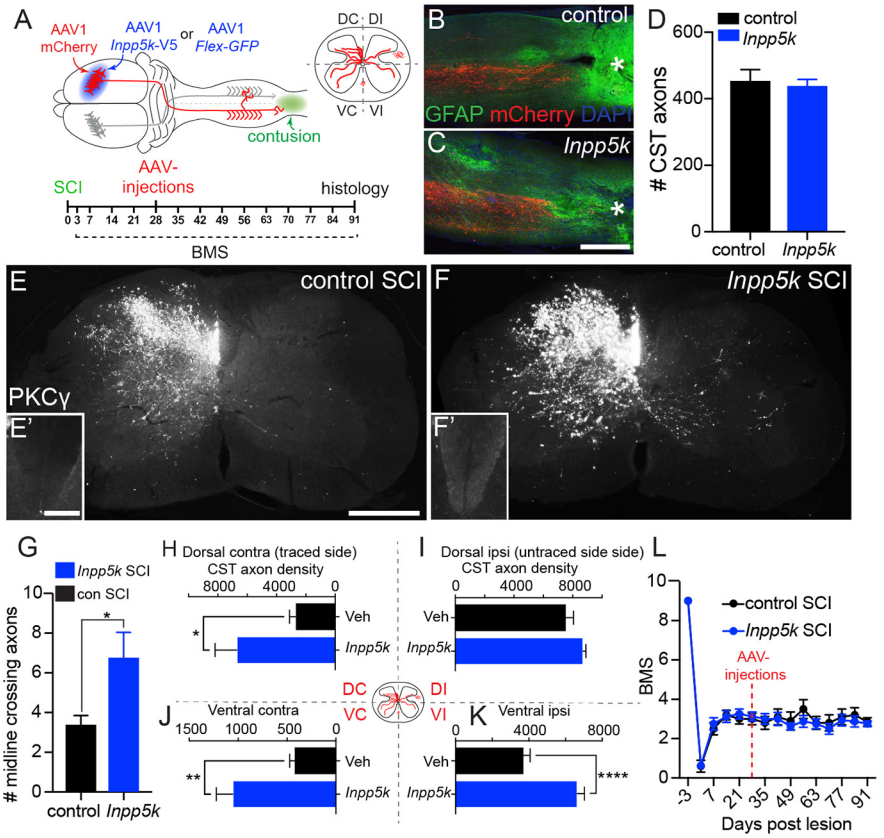

Figure 7. *Inpp5k* increases CST sprouting after chronic contusion injury. ***A***, Schematic shows bilateral T11 contusion injury (green) and delivery of AAV1 mCherry and *Inpp5k*-V5 into the right side of motor cortex. Inset schematic shows quadrants of cord analyzed and the experimental timeline: AVVs were delivered 28 d post-SCI. ***B***, ***C***, Photomicrographs show horizontal sections through the lesion site 13 weeks after severe contusion injury in control mice (mCherry$^+$ CST axons, red; GFAP, green; asterisks indicate lesion site; ***B***) and *Inpp5k*-treated mice (***C***). No mCherry$^+$ CST axons grew into or past the lesion site. ***D***, No significant differences were found in the number of mCherry$^+$ CST axons counted in the C4 spinal segment between treatment groups (data shown are the average number of puncta ± SEM). ***B***, ***E***, Photomicrographs show transverse sections through C6 showing mCherry$^+$ CST axon labeling in control SCI (***E***; $n = 8$) and *Inpp5k* SCI (***B***; $n = 8$). ***E′***, ***F′***, Insets show the complete absence of PKC$^\gamma$-IR in injured mice. ***H***, ***J***, ***K***, Densitometric analysis of mCherry$^+$ CST axons in gray matter showed that *Inpp5k* treatment was significant in the DC quadrant (***H***; $t_{(8.116)} = 2.597$, $^*p = 0.0314$, unpaired t test with Welch's correction), the VC quadrant (***J***; $t_{(8.270)} = 3.600$, $^{**}p = 0.0066$, unpaired t test with Welch's correction), and the VI quadrant (***K***; $t_{(13.88)} = 5.530$, $^{****}p < 0.0001$, unpaired t test with Welch's correction). ***I***, There was no effect of *Inpp5k* on CST density in the DI quadrant. ***G***, Data are shown as the average mCherry$^+$ CST density ± SEM. *Inpp5k* increased the number of midline crossing CST axons compared with control ($t_{(14)} = 2.348$, $p = 0.034$, unpaired two-tailed t test; data shown are the average number of axons ± SEM). ***L***, Behavioral assessment using the BMS revealed that there was no significance between *Inpp5k*-treated and control-treated SCI mice (two-way ANOVA with repeated measures with Bonferroni's *post hoc* comparisons test, $p > 0.05$; data shown are the average BMS score ± SEM). Scale bars: ***C***, 2 mm; ***E***, 500 µm; ***E′***, 100 µm.

Inpp5k increases sprouting of CST axons following chronic contusion SCI

To determine whether *Inpp5k* could stimulate sprouting and/or regeneration of CST axons after chronic contusion injury, we completed severe 75 kdyn T11 contusion injuries in wild-type mice, waited 28 d for hindlimb motor recovery to plateau, and then delivered either AAV-*Inpp5k*-V5 and AAV-mCherry or AAV-FLEX-GFP (control) and AAV-mCherry into the right motor cortex. Motor function was assessed with the BMS for an additional 9 weeks (Fig. 7*A*). Horizontal sections through midthoracic cord showed mCherry$^+$ CST axons regenerating up to the penumbra of the GFAP-enriched lesion site in both control (Fig. 7*B*) and *Inpp5k*-treated (Fig. 7*C*) mice; however, no CST axons were seen penetrating through the lesion and entering the spinal caudal to the lesion site in either group. Analysis of tissue sparing around the lesion confirmed that there was no difference between groups ($t_{(1.037)} = 13$, $p = 0.319$, unpaired two-tailed t test). There was no significant difference in the number of CST axons labeled in the C5 dorsal columns between the groups (Fig. 7*D*), confirming that *Inpp5k* had no effect on the health or survival of chronically injured CST axons. To explore whether the delivery of *Inpp5k* could stimulate the sprouting of CST axons in the cervical cord after chronic contusion injury, we completed an identical densitometric analysis

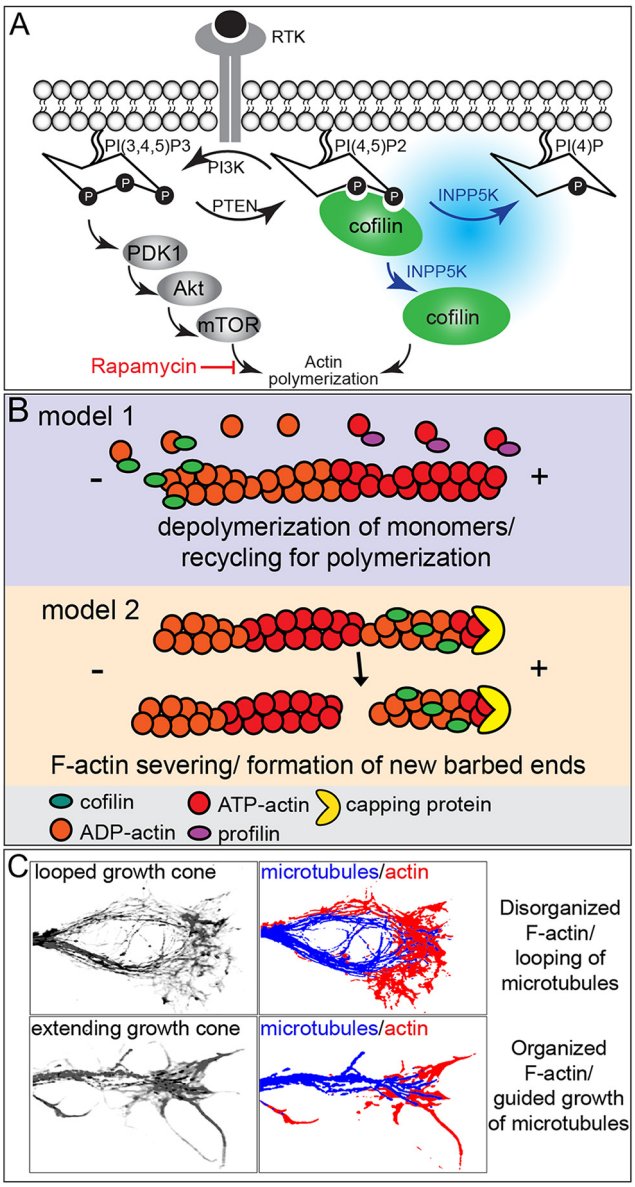

Figure 8. Model for the mechanism of *Inpp5k*-induced axon extension. PI3K is activated by growth factors binding to receptor tyrosine kinases phosphorylating PI(4,5)P2 forming PI(3,4,5)P3, initiating mTOR-dependent (rapamycin sensitive) actin polymerization and enhanced neurite outgrowth. ***A***, Dephosphorylation of basal levels of $PI(4,5)P_2$ to PI(4)P by *Inpp5k* leads to the unbinding of a pool of active cofilin from the plasma membrane that can engage in cytoskeletal remodeling (Saarikangas et al., 2010). Two predominant hypothetical models by which cofilin regulates cytoskeletal remodeling, leading to protrusion and extension of growth cones. In model 1, cofilin binds to ATP-actin at the pointed end of filaments, depolymerizing them. This increases the availability of monomers converted to ATP-actin and polymerization by profilin. In model 2, capping proteins prevent polymerization. ***B***, Cofilin severs F-actin creating new barbed ends for polymerization. ***C***, LUT (look-up table) confocal images of paused looped growth cone (top left) and extending the growth cone (bottom left). Right, Diagram of morphology of microtubules (blue) and F-actin (red). In the looped paused growth cone (top right), F-actin is disorganized, leading to abnormal microtubule growth. In the extending growth cone (bottom right), F-actin is organized, which directs microtubules in a radial orientation leading to directional growth.

at >13 weeks postlesion. Transverse sections of mCherry$^+$ CST axons can be seen densely innervating one side of the spinal cord in both control (Fig. 7*E*) and *Inpp5k*-treated mice (Fig. 7*F*). The absence of PKCγ-IR in the L4 spinal cord confirmed that the contusion ablated the CST in its entirety (Fig. 7*E*′,*F*′). *Inpp5k* treatment increased the density of mCherry$^+$ CST axons in all quadrants on both sides of the cord compared with control-treated mice (Fig. 7*H*,*I*). Additionally, *Inpp5k* treatment also increased the number of mCherry$^+$ CST axons crossing the midline (Fig. 7*G*). However, hindlimb motor scores using the BMS revealed that once mice had plateaued at 28 d, *Inpp5k* did not stimulate further motor recovery (Fig. 7*L*). In summary, we found that *Inpp5k* overexpression enhances the sprouting of chronically injured CST axons rostral to the lesion but did not stimulate the regeneration of cut axons after chronic contusion injury.

Discussion

Transcriptional screening of intact sprouting adult CSNs after PyX revealed an enrichment of genes in the 3-PID pathway. Here, we tested whether *Inpp5k* could stimulate CST axon growth after preclinical models of CNS trauma. We show the following: (1) that *Inpp5k* increases axon outgrowth of cortical neurons *in vitro* in part by increasing the availability of active nonphosphorylated cofilin within labile axonal growth cones; (2) that the overexpression of *Inpp5k* enhances the plasticity of intact CSNs after PyX and cortical stroke; (3) that *Inpp5k* increases the sprouting of CSNs rostral to acute severe thoracic contusion SCI; (4) that *Inpp5k* increases the sprouting of CSNs in the cervical spinal cord when delivered 4 weeks after severe contusion injury; and (5) that *Inpp5k* does not increase the regeneration of damaged CSNs after SCI. From these data, we can draw the following several conclusions: first, *Inpp5k* is a novel pro-axon growth modulator in adult CSNs capable of driving the growth of CST arbors before and after injury; second, confirmation that transcriptional profiling of adult sprouting CSNs is a robust approach to identifying novel axon growth activators; and, finally, that using combined localized retrograde tracing and transcriptional profiling may specifically identify pro-axon growth processes unique to a subset of neurons whose terminals are extending into the traced area and are not generalizable axon growth activators, thus suggesting that comprehensive CST repair will require CSN subtype-specific interventions.

Inpp5k mechanism of axon growth

Inpp5k is part of the 3-PID that is critical in modulating the activity of PI3K. Upon growth factor binding, PI3K catalyzes the conversion of PI(4,5)P2 to PI(3,4,5)P3 and, via PDK1-dependent Akt phosphorylation, results in mTOR activation (Ooms et al., 2009). The PI3K–mTOR pathway controls cell survival and axogenic protein synthesis during development (Fonseca et al., 2014; Berry et al., 2016). The 3-phosphatase *Pten* terminates PI(3,4,5)P3 synthesis. *Pten* levels increase during development and into adulthood and restrict axon growth signaling via mTOR. Additionally, *Pten* stimulates robust axon regeneration after SCI (Park et al., 2008; Liu et al., 2010; Ohtake et al., 2014). PI(3,4,5)P3 is also degraded by 5-phosphatases, including *Inpp5k*, to produce PI(3,4)P2, which also activates PDK1/Akt (Ooms et al., 2009). Thus, 5-phosphatases could elevate free PI(3,4)P2 and thus stimulate axon growth via mTOR. However, the mTOR inhibitor rapamycin failed to abrogate the progrowth effects of *Inpp5k in vitro*, thus pointing to an mTOR-independent mechanism.

PI(4,5)P2 has also been shown to bind the actin polymerizing domain of cofilin, retaining it in the plasma membrane (Yonezawa et al., 1990, 1991). For cofilin to participate in actin remodeling, it needs to be released from the plasma membrane. Indeed, the release of cofilin from PI(4,5)P2 has been shown *in vitro* to bind severed F-actin and lead to actin polymerization

and lamellipodia formation (van Rheenen et al., 2007). Crucially, this study also showed that recombinant 5-phospatase activity was sufficient to release active cofilin into the cytosol. Active cofilin has previously been shown to drive neurite formation and elongation *in vitro* (Endo et al., 2003; Letourneau, 2009; Flynn et al., 2012; Dupraz et al., 2019) and has been shown to be necessary for the regeneration of sensory neurons in the CNS *in vivo* (Tedeschi et al., 2019). Here we show that the overexpression of *Inpp5k* in embryonic cortical neurons increased the density of active cofilin in growth cones (Fig. 2*O*) and enhanced neurite outgrowth. Thus, we propose that *Inpp5k* dephosphorylates $PI(4,5)P_2$, releasing cofilin in its active state to promote actin remodeling (Fig. 8*A*) via either F-actin depolymerization or F-actin severing (Fig. 8*B*).

The morphology of growth cones transfected with *Inpp5k* further supports this mechanism. *Inpp5k* overexpression prevented a looped morphology seen in paused growth cones in favor of extending growth cones, consistent with previous work (Endo et al., 2003; Flynn et al., 2012). F-actin microtubule interactions are an important driving force for microtubule orientation and extension of growth cones. Microtubules penetrate the growth cone periphery where they align with actin filament bundles (Dent and Kalil, 2001). Growth cones that are paused display a tightly bundled loop (Fig. 8*B*,*E*). Cofilin promotes severing of F-actin and the subsequent actin turnover allows the radial orientation of F-actin (Flynn et al., 2012). Microtubules associated with the actin filaments are then guided in an extending orientation. In the absence of cofilin, F-actin becomes disorganized, leading to looped and disorganized trajectories. *Inpp5k* expression increased polymerizing microtubules guided by filipodia in the periphery of growth cones. The microtubule protrusion and polymerization at the leading end of the growth cone leads to accelerated axon growth (Dupraz et al., 2019). Thus, we propose that *Inpp5k* increases axon extension via cytoskeletal remodeling and subsequently guided microtubule extension.

Inpp5k enhances axon growth *in vivo*

Previously, we showed that *Inpp5k* enhanced neurite outgrowth in DIV3 cortical neuron cultures (Fink et al., 2017). Here we explored whether overexpression of *Inpp5k* could elevate the growth of intact and axotomized neurons in preclinical models of CNS trauma. *Inpp5k* stimulated significant sprouting of intact CST arbors throughout spinal gray matter on the intact and denervated side of the cervical spinal cord. Despite robust sprouting into the denervated ventral horn, *Inpp5k*-treated mice did not show an increase or decrement in functional recovery versus controls; however, grid-walking analysis may not have been sensitive enough to detect small but important functional gains associated with increased compensatory CST sprouting. Nonetheless, these observations are consistent with studies that target monogenic manipulation of intact CSNs including *Lppr1* overexpression (Fink et al., 2017), *Klf6* overexpression (Kramer et al., 2021), *Sox11* overexpression (Wang et al., 2015), and *Pten* deletion (Geoffroy et al., 2015). These studies show that targeting each of these genes in isolation increased the sprouting of intact CSNs post-PyX but did not elevate functional recovery. Similarly, after stroke, *Inpp5k* overexpression enhanced the sprouting of intact CSNs without enhancing functional recovery. It remains possible that in the absence of additional stimuli that can guide labile CST arbors to functionally appropriate postsynaptic targets, such as rehabilitative training (Wahl et al., 2014; Serradj et al., 2017; Loy et al., 2018; Torres-Espín et al., 2018; Loy and Bareyre, 2019), all monogenic interventions may remain therapeutically suboptimal (Weishaupt et al., 2013; Jayaprakash et al., 2016). Nevertheless, targeting compensatory growth of intact CST axons to restore function after partial SCI remains of high therapeutic value because of the observed behavioral benefits of constitutive neuronal deletion of *Ngr1* (Cafferty and Strittmatter, 2006; Fink et al., 2017), neuroaxial delivery of anti-*Ngr1* (Wang et al., 2020), anti-NogoA-specific antibodies (Thallmair et al., 1998; Freund et al., 2007), chondroitinase ABC (Bradbury et al., 2002; Starkey et al., 2012; Rosenzweig et al., 2019), and combined targeting of *Pten* and *Socs3* (Jin et al., 2015).

To assess whether *Inpp5k* could also stimulate regeneration of lesioned CST axons, we overexpressed *Inpp5k* or FLEX-GFP (control) in adult mice either 2 weeks (acute treatment) before or 4 weeks after (chronic treatment) a severe bilateral thoracic contusion injury. Neither acute nor delayed treatment enhanced the regeneration of CST axons into or past the lesion site. However, we observed significant sprouting of CST arbors in the cervical gray matter, with many segments rostral to the lesion after acute and chronic contusion in *Inpp5k*-treated mice. These data cannot determine whether the sprouting axons were intact cervical CST axons or axotomized lumbar axons. Nonetheless, the robust CST sprouting observed after contusion injury shows that *Inpp5k* can stimulate and support axon growth in four different complex CNS injury environments.

Corticospinal neuron subtype-specific therapies?

We profiled intact, sprouting adult CSNs after PyX to identify novel intrinsic axon growth activators *Lppr1* and *Inpp5k*. Overexpression of both targets resulted in significant sprouting of CST axons into the cervical spinal cord, but not the regeneration of axotomized CST axons through the lesion site after thoracic contusion injury. These data raise an important question regarding the homogeneity of CSNs. Our screen was completed in *crym*-GFP transgenic mice treated with retrograde tracers injected into the contralateral cervical enlargement after PyX. While the *crym*-GFP transgenic line is superior in labeling CSNs versus tracers, it may not represent complete CSN coverage (Arlotta et al., 2005; Fink et al., 2015; Golan et al., 2021) and could preferentially label CSNs innervating the cervical cord. Thus, the bulk sequencing from our screen would have undersampled plastic lumbar CSNs. Additionally, we injected a retrograde tracer into the intact cervical spinal cord to identify CSNs whose arbors had sprouted across the midline. This combination of approaches may have resulted in the identification of forelimb-specific CSN growth activators. Indeed, we observed sprouting of CST axons in the cervical cord after PyX, stroke, and acute and chronic contusion injury, yet no growth of CST axons in and around the caudal thoracic segments. These data highlight the intriguing possibility that anatomically distinct CST terminal regions (i.e., lumbar and cervical enlargements) may require disparate therapeutic interventions to stimulate axon growth. Therefore, a comprehensive understanding of the unique molecular profile of anatomic subregions of CSN projections in the spinal cord may be required to guide therapeutic interventions. that require focus on specific regions of the spinal cord, for instance targeting lumbar CSNs after thoracic SCI.

References

Arlotta P, Molyneaux BJ, Chen J, Inoue J, Kominami R, Macklis JD (2005) Neuronal subtype-specific genes that control corticospinal motor neuron development in vivo. Neuron 45:207–221.

Basso DM, Fisher LC, Anderson AJ, Jakeman LB, McTigue DM, Popovich PG (2006) Basso Mouse Scale for locomotion detects differences in

recovery after spinal cord injury in five common mouse strains. J Neurotrauma 23:635–659.
Berry M, Ahmed Z, Morgan-Warren P, Fulton D, Logan A (2016) Prospects for mTOR-mediated functional repair after central nervous system trauma. Neurobiol Dis 85:99–110.
Blackmore MG, Moore DL, Smith RP, Goldberg JL, Bixby JL, Lemmon VP (2010) High content screening of cortical neurons identifies novel regulators of axon growth. Mol Cell Neurosci 44:43–54.
Bradbury EJ, Burnside ER (2019) Moving beyond the glial scar for spinal cord repair. Nat Commun 10:3879.
Bradbury EJ, Moon LD, Popat RJ, King VR, Bennett GS, Patel PN, Fawcett JW, McMahon SB (2002) Chondroitinase ABC promotes functional recovery after spinal cord injury. Nature 416:636–640.
Buchser WJ, Slepak TI, Gutierrez-Arenas O, Bixby JL, Lemmon VP (2010) Kinase/phosphatase overexpression reveals pathways regulating hippocampal neuron morphology. Mol Syst Biol 6:391.
Cafferty WB, Strittmatter SM (2006) The Nogo-Nogo receptor pathway limits a spectrum of adult CNS axonal growth. J Neurosci 26:12242–12250.
Cafferty WB, Duffy P, Huebner E, Strittmatter SM (2010) MAG and OMgp synergize with Nogo-A to restrict axonal growth and neurological recovery after spinal cord trauma. J Neurosci 30:6825–6837.
Curcio M, Bradke F (2018) Axon regeneration in the central nervous system: facing the challenges from the inside. Annu Rev Cell Dev Biol 34:495–521.
Dent EW, Kalil K (2001) Axon branching requires interactions between dynamic microtubules and actin filaments. J Neurosci 21:9757–9769.
Dupraz S, Hilton BJ, Husch A, Santos TE, Coles CH, Stern S, Brakebusch C, Bradke F (2019) RhoA controls axon extension independent of specification in the developing brain. Curr Biol 29:3874–3886.e9.
Endo M, Ohashi K, Sasaki Y, Goshima Y, Niwa R, Uemura T, Mizuno K (2003) Control of growth cone motility and morphology by LIM kinase and Slingshot via phosphorylation and dephosphorylation of cofilin. J Neurosci 23:2527–2537.
Festing MF, DG Altman (2002) Guidelines for the design and statistical analysis of experiments using laboratory animals. ILAR J 43:244–258.
Fink KL, Strittmatter SM, Cafferty WB (2015) Comprehensive corticospinal labeling with mu-crystallin transgene reveals axon regeneration after spinal cord trauma in *ngr1*$^{-/-}$ mice. J Neurosci 35:15403–15418.
Fink KL, López-Giráldez F, Kim IJ, Strittmatter SM, Cafferty WBJ (2017) Identification of intrinsic axon growth modulators for intact CNS neurons after injury. Cell Rep 18:2687–2701.
Flynn KC, Hellal F, Neukirchen D, Jacob S, Tahirovic S, Dupraz S, Stern S, Garvalov BK, Gurniak C, Shaw AE, Meyn L, Wedlich-Söldner R, Bamburg JR, Small JV, Witke W, Bradke F (2012) ADF/cofilin-mediated actin retrograde flow directs neurite formation in the developing brain. Neuron 76:1091–1107.
Fonseca BD, Smith EM, Yelle N, Alain T, Bushell M, Pause A (2014) The ever-evolving role of mTOR in translation. Semin Cell Dev Biol 36:102–112.
Freund P, Wannier T, Schmidlin E, Bloch J, Mir A, Schwab ME, Rouiller EM (2007) Anti-Nogo-A antibody treatment enhances sprouting of corticospinal axons rostral to a unilateral cervical spinal cord lesion in adult macaque monkey. J Comp Neurol 502:644–659.
Geoffroy CG, Lorenzana AO, Kwan JP, Lin K, Ghassemi O, Ma A, Xu N, Creger D, Liu K, He Z, Zheng B (2015) Effects of PTEN and Nogo codeletion on corticospinal axon sprouting and regeneration in mice. J Neurosci 35:6413–6428.
Golan N, Kauer S, Ehrlich DB, Ravindra N, van Dijk D, Cafferty WB (2021) Single-cell transcriptional profiling of the adult corticospinal tract reveals forelimb and hindlimb molecular specialization. bioRxiv. Advance online publication. Retrieved February 8, 2022.
Harrison M, O'Brien A, Adams L, Cowin G, Ruitenberg MJ, Sengul G, Watson C (2013) Vertebral landmarks for the identification of spinal cord segments in the mouse. Neuroimage 68:22–29.
Huebner EA, Kim BG, Duffy PJ, Brown RH, Strittmatter SM (2011) A multidomain fragment of Nogo-A protein is a potent inhibitor of cortical axon regeneration via Nogo receptor 1. J Biol Chem 286:18026–18036.
Ijuin T, Mochizuki Y, Fukami K, Funaki M, Asano T, Takenawa T (2000) Identification and characterization of a novel inositol polyphosphate 5-phosphatase. J Biol Chem 275:10870–10875.
Jayaprakash N, Wang Z, Hoeynck B, Krueger N, Kramer A, Balle E, Wheeler DS, Wheeler RA, Blackmore MG (2016) Optogenetic interrogation of functional synapse formation by corticospinal tract axons in the injured spinal cord. J Neurosci 36:5877–5890.
Jin D, Liu Y, Sun F, Wang X, Liu X, He Z (2015) Restoration of skilled locomotion by sprouting corticospinal axons induced by co-deletion of PTEN and SOCS3. Nat Commun 6:8074.
Kramer AA, Olson GM, Chakraborty A, Blackmore MG (2021) Promotion of corticospinal tract growth by KLF6 requires an injury stimulus and occurs within four weeks of treatment. Exp Neurol 339:113644.
Kucher K, Johns D, Maier D, Abel R, Badke A, Baron H, Thietje R, Casha S, Meindl R, Gomez-Mancilla B, Pfister C, Rupp R, Weidner N, Mir A, Schwab ME, Curt A (2018) First-in-man intrathecal application of neurite growth-promoting anti-Nogo-A antibodies in acute spinal cord injury. Neurorehabil Neural Repair 32:578–589.
Labat-gest V, Tomasi S (2013) Photothrombotic ischemia: a minimally invasive and reproducible photochemical cortical lesion model for mouse stroke studies. J Vis Exp (76):50370.
Letourneau PC (2009) Actin in axons: stable scaffolds and dynamic filaments. Results Probl Cell Differ 48:65–90.
Lindborg JA, Tran NM, Chenette DM, DeLuca K, Foli Y, Kannan R, Sekine Y, Wang X, Wollan M, Kim IJ, Sanes JR, Strittmatter SM (2021) Optic nerve regeneration screen identifies multiple genes restricting adult neural repair. Cell Rep 34:108777.
Liu K, Lu Y, Lee JK, Samara R, Willenberg R, Sears-Kraxberger I, Tedeschi A, Park KK, Jin D, Cai B, Xu B, Connolly L, Steward O, Zheng B, He Z (2010) PTEN deletion enhances the regenerative ability of adult corticospinal neurons. Nat Neurosci 13:1075–1081.
Loy K, Bareyre FM (2019) Rehabilitation following spinal cord injury: how animal models can help our understanding of exercise-induced neuroplasticity. Neural Regen Res 14:405–412.
Loy K, Schmalz A, Hoche T, Jacobi A, Kreutzfeldt M, Merkler D, Bareyre FM (2018) Enhanced voluntary exercise improves functional recovery following spinal cord injury by impacting the local neuroglial injury response and supporting the rewiring of supraspinal circuits. J Neurotrauma 35:2904–2915.
Moore DL, Blackmore MG, Hu Y, Kaestner KH, Bixby JL, Lemmon VP, Goldberg JL (2009) KLF family members regulate intrinsic axon regeneration ability. Science 326:298–301.
Ohtake Y, Park D, Abdul-Muneer PM, Li H, Xu B, Sharma K, Smith GM, Selzer ME, Li S (2014) The effect of systemic PTEN antagonist peptides on axon growth and functional recovery after spinal cord injury. Biomaterials 35:4610–4626.
Ooms LM, Horan KA, Rahman P, Seaton G, Gurung R, Kethesparan DS, Mitchell CA (2009) The role of the inositol polyphosphate 5-phosphatases in cellular function and human disease. Biochem J 419:29–49.
Park KK, Liu K, Hu Y, Smith PD, Wang C, Cai B, Xu B, Connolly L, Kramvis I, Sahin M, He Z (2008) Promoting axon regeneration in the adult CNS by modulation of the PTEN/mTOR pathway. Science 322:963–966.
Park SJ, Borghuis BG, Rahmani P, Zeng Q, Kim IJ, Demb JB (2015) Function and circuitry of VIP^{+} interneurons in the mouse retina. J Neurosci 35:10685–10700.
Rosenzweig ES, Salegio EA, Liang JJ, Weber JL, Weinholtz CA, Brock JH, Moseanko R, Hawbecker S, Pender R, Cruzen CL, Iaci JF, Caggiano AO, Blight AR, Haenzi B, Huie JR, Havton LA, Nout-Lomas YS, Fawcett JW, Ferguson AR, Beattie MS, et al (2019) Chondroitinase improves anatomical and functional outcomes after primate spinal cord injury. Nat Neurosci 22:1269–1275.
Saarikangas J, Zhao H, Lappalainen P (2010) Regulation of the actin cytoskeleton-plasma membrane interplay by phosphoinositides. Physiol Rev 90:259–289.
Schwab ME, Strittmatter SM (2014) Nogo limits neural plasticity and recovery from injury. Curr Opin Neurobiol 27:53–60.
Sekine Y, Lin-Moore A, Chenette DM, Wang X, Jiang Z, Cafferty WB, Hammarlund M, Strittmatter SM (2018) Functional genome-wide screen identifies pathways restricting central nervous system axonal regeneration. Cell Rep 23:415–428.
Serradj N, Agger SF, Hollis ER 2nd (2017) Corticospinal circuit plasticity in motor rehabilitation from spinal cord injury. Neurosci Lett 652:94–104.
Starkey ML, Barritt AW, Yi PK, Davies M, Hamers FPT, McMahon SB, Bradbury EJ (2005) Assessing behavioural function following a pyramidotomy lesion of the corticospinal tract in adult mice. Exp Neurol 195:524–539.

Starkey ML, Bartus K, Barritt AW, Bradbury EJ (2012) Chondroitinase ABC promotes compensatory sprouting of the intact corticospinal tract and recovery of forelimb function following unilateral pyramidotomy in adult mice. Eur J Neurosci 36:3665–3678.

Tedeschi A, Dupraz S, Curcio M, Laskowski CJ, Schaffran B, Flynn KC, Santos TE, Stern S, Hilton BJ, Larson MJE, Gurniak CB, Witke W, Bradke F (2019) ADF/cofilin-mediated actin turnover promotes axon regeneration in the adult CNS. Neuron 103:1073–1085.e6.

Thallmair M, Metz GA, Z'Graggen WJ, Raineteau O, Kartje GL, Schwab ME (1998) Neurite growth inhibitors restrict plasticity and functional recovery following corticospinal tract lesions. Nat Neurosci 1:124–131.

Torres-Espín A, Beaudry E, Fenrich K, Fouad K (2018) Rehabilitative training in animal models of spinal cord injury. J Neurotrauma 35:1970–1985.

Tran NM, Shekhar K, Whitney IE, Jacobi A, Benhar I, Hong G, Yan W, Adiconis X, Arnold ME, Lee JM, Levin JZ, Lin D, Wang C, Lieber CM, Regev A, He Z, Sanes JR (2019) Single-cell profiles of retinal ganglion cells differing in resilience to injury reveal neuroprotective genes. Neuron 104:1039–1055.e12.

van Rheenen J, Song X, van Roosmalen W, Cammer M, Chen X, Desmarais V, Yip SC, Backer JM, Eddy RJ, Condeelis JS (2007) EGF-induced PIP2 hydrolysis releases and activates cofilin locally in carcinoma cells. J Cell Biol 179:1247–1259.

van Rheenen J, Condeelis J, Glogauer M (2009) A common cofilin activity cycle in invasive tumor cells and inflammatory cells. J Cell Sci 122:305–311.

Venkatesh I, Mehra V, Wang Z, Califf B, Blackmore MG (2018) Developmental chromatin restriction of pro-growth gene networks acts as an epigenetic barrier to axon regeneration in cortical neurons. Dev Neurobiol 78:960–977.

Venkatesh I, Mehra V, Wang Z, Simpson MT, Eastwood E, Chakraborty A, Beine Z, Gross D, Cabahug M, Olson G, Blackmore MG (2021) Co-occupancy analysis reveals novel transcriptional synergies for axon growth. bioRxiv.

Wahl AS, Omlor W, Rubio JC, Chen JL, Zheng H, Schröter A, Gullo M, Weinmann O, Kobayashi K, Helmchen F, Ommer B, Schwab ME (2014) Neuronal repair. Asynchronous therapy restores motor control by rewiring of the rat corticospinal tract after stroke. Science 344:1250–1255.

Wang JT, Kunzevitzky NJ, Dugas JC, Cameron M, Barres BA, Goldberg JL (2007) Disease gene candidates revealed by expression profiling of retinal ganglion cell development. J Neurosci 27:8593–8603.

Wang X, Zhou T, Maynard GD, Terse PS, Cafferty WB, Kocsis JD, Strittmatter SM (2020) Nogo receptor decoy promotes recovery and corticospinal growth in non-human primate spinal cord injury. Brain 143:1697–1713.

Wang Z, Reynolds A, Kirry A, Nienhaus C, Blackmore MG (2015) Overexpression of Sox11 promotes corticospinal tract regeneration after spinal injury while interfering with functional recovery. J Neurosci 35:3139–3145.

Weishaupt N, Li S, Di Pardo A, Sipione S, Fouad K (2013) Synergistic effects of BDNF and rehabilitative training on recovery after cervical spinal cord injury. Behav Brain Res 239:31–42.

Yonezawa N, Nishida E, Iida K, Yahara I, Sakai H (1990) Inhibition of the interactions of cofilin, destrin, and deoxyribonuclease I with actin by phosphoinositides. J Biol Chem 265:8382–8386.

Yonezawa N, Homma Y, Yahara I, Sakai H, Nishida E (1991) A short sequence responsible for both phosphoinositide binding and actin binding activities of cofilin. J Biol Chem 266:17218–17221.

Zhang J, Yang D, Huang H, Sun Y, Hu Y (2018) Coordination of necessary and permissive signals by PTEN inhibition for CNS axon regeneration. Front Neurosci 12:558.

Zou Y, Stagi M, Wang X, Yigitkanli K, Siegel CS, Nakatsu F, Cafferty WB, Strittmatter SM (2015) Gene-silencing screen for mammalian axon regeneration identifies Inpp5f (Sac2) as an endogenous suppressor of repair after spinal cord injury. J Neurosci 35:10429–10439.